Chemical Engineering Journal 525 (2025) 170323

Contents lists available at ScienceDirect

Chemical Engineering Journal

journal homepage: www.elsevier.com/locate/cej

Decoding the role of oxygen species in glucose oxidation to glucaric acid on AuPt/ZrO_2: A kinetic and experimental study

Žan Lavrič [a,b], Sašo Gyergyek [c], Blaž Likozar [a], Miha Grilc [a,b,*]

[a] Department of Catalysis and Chemical Reaction Engineering, National Institute of Chemistry, Hajdrihova 19, SI-1000, Ljubljana, Slovenia
[b] University of Nova Gorica, Vipavska 13, SI-5000, Nova Gorica, Slovenia
[c] Department of Synthesis of Materials, Jožef Stefan Institute, Jamova Cesta 39, 1000, Ljubljana, Slovenia

ARTICLE INFO

Keywords:
Selective glucose oxidation
Heterogeneous catalysis
Glucaric acid
Kinetic modelling
Model validation

ABSTRACT

This study presents a detailed kinetic investigation of the reaction mechanisms of selective glucose oxidation (SO) to glucaric acid with AuPt/ZrO_2 catalyst under aqueous, base-free conditions. A detailed experimental design was carried out with all intermediates (gluconic, glucuronic and glucaric acid) of the reaction pathway in order to accurately determine the rate of the individual surface reactions. A total of 25 experiments (with 700 experimentally determined concentration points) were performed and used as an extensive database to formulate a kinetic model describing various kinetic phenomena; gas-liquid-solid transfer of O_2 and a detailed surface kinetics with C_6 and oxygen species. Reaction temperature, time, O_2 pressure and reactant or intermediates concentration were varied. Among all performed experiments, the highest glucaric acid yield (77 %, starting reactant: glucuronic acid) was determined for a base-free, selective O_2 oxidation. Predictive model and validation experiment revealed much higher reaction rate constants for O*-assisted oxidation of glucose ($k_{100\ °C} = 120\ min^{-1}$) compared to gluconic acid ($k_{100\ °C} = 51\ min^{-1}$). The formation of the latter is fast and selective in a wide temperature window, whereas the formation of glucaric acid requires elevated temperatures. The activation energy of glucaric acid formation from gluconic acid (59 kJ mol^{-1}) is a bit higher, than its decomposition (56 kJ mol^{-1}), which compromises glucaric acid yields across the entire temperature range.

1. Introduction

The urgent need for sustainable alternatives to fossil fuels, combined with the environmental problems of conventional industrial processes, has put biomass conversion at the center of attention in the recent decades. The shift to bio-based and renewable chemical feedstocks not only reduces our dependence on finite fossil fuels, but also opens up a wide range of materials that support both environmental sustainability and economic resilience. This transition is a crucial step towards greener, more sustainable future [1].

A promising approach for a sustainable use of biomass is the use of heterogeneous catalysts for key transformation reactions such as hydrogenation, dehydroxylation, dehydration, hydrolysis and oxidation [2]. The latter, also termed selective oxidation (SO) of biomass or its derivatives has attracted considerable attention, due to its ability to convert biomass into higher-value platform chemicals with functional groups such as formyl (–CHO), carbonyl (C=O) and carboxyl (-COOH). Over the past decades, a variety of substrates, catalysts, experimental conditions and characterization techniques have been explored, resulting in a large and diversified database [3,4]. In addition to experimental advances, mechanistic studies have provided valuable insights into the complex pathways of oxidation reactions and enabled the development of predictive mathematical models [5–7]. However, despite the wealth of data available, many aspects of SO mechanisms remain unresolved and are the subject of ongoing debate. This underlines the need for future research to fully elucidate and optimize these processes.

The SO mechanisms of alcohols and aldehydes on metallic nanoparticles (NP) were concisely reviewed by Davies et al. [5]. In short, primary alcohol adsorbs on a metallic active site and forms a metal-alkoxide and a metal-hydride, followed by β-hydride elimination to obtain carbonyl groups and regenerate the active site. During the oxidation of aldehydes, geminal diols are formed in the liquid phase before similar dehydrogenation steps take place. However, the dehydrogenation of the hydrogen atom does not necessarily require an

* Corresponding author at: Department of Catalysis and Chemical Reaction Engineering, National Institute of Chemistry, Hajdrihova 19, SI-1000, Ljubljana, Slovenia.
E-mail address: miha.grilc@ki.si (M. Grilc).

https://doi.org/10.1016/j.cej.2025.170323
Received 12 May 2025; Received in revised form 1 October 2025; Accepted 29 October 2025
Available online 30 October 2025

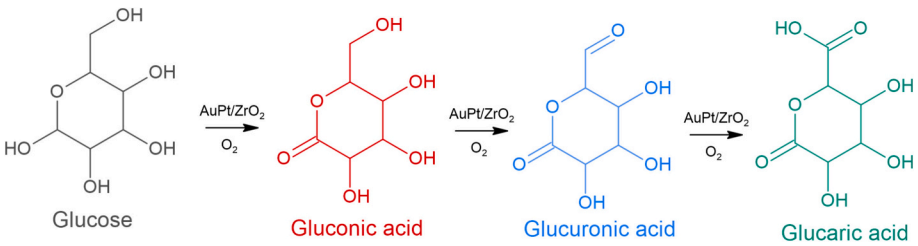

Fig. 1. Simplified reaction scheme for selective GLC oxidation to GA.

Table 1
Exact reaction equations used in kinetic model.

Reaction #	Reaction equation	Kinetic equation
1	$O_2^* + H_2O \rightarrow 2OH^* + O^*$	$r_1^{surf} = k_1^{surf} \bullet \Theta_{O_2} \bullet \Theta_X^2$
2	$O^* + H_2O \rightarrow 2OH^*$	$r_2^{surf} = k_2^{surf} \bullet \Theta_O \bullet \Theta_X$
3	$GLC^* + OH^* \rightarrow GU^*$	$r_3^{surf} = k_3^{surf} \bullet \Theta_{GLC} \bullet \Theta_{OH}$
4	$GU^* + O^* \rightarrow GLU^*$	$r_4^{surf} = k_4^{surf} \bullet \Theta_{GU} \bullet \Theta_O$
5	$GLU^* + OH^* \rightarrow GA^*$	$r_5^{surf} = k_5^{surf} \bullet \Theta_{GLU} \bullet \Theta_{OH}$
6	$GA^* + OH^* \rightarrow Others^*$	$r_6^{surf} = k_6^{surf} \bullet \Theta_{GA} \bullet \Theta_{OH}$
7	$2OH^* \rightarrow O^* + H_2O$	$r_7^{surf} = k_7^{surf} \bullet \Theta_{OH}^2$

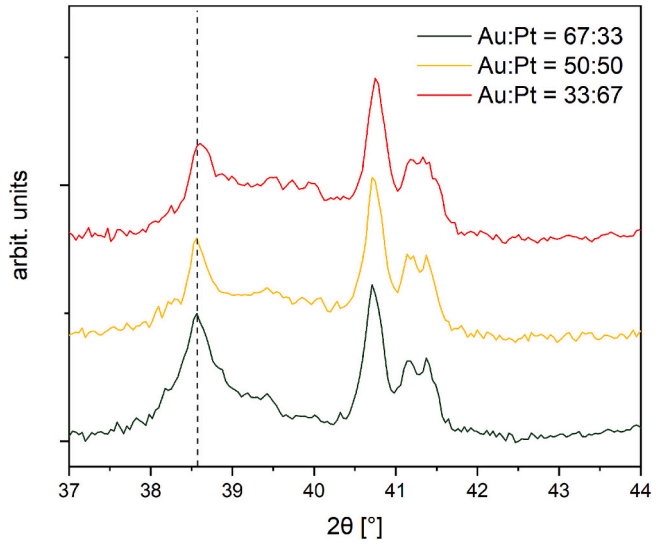

Fig. 2. Overlaid XRD diffractograms of all three synthesized materials – magnified region, where Au peak at 38° 2Θ, is not present.

adjacent free active metallic site. In an earlier study [6] by the same research group, an aqueous glycerol to glyceric acid oxidation with O_2 was performed with Au/C and Pt/C catalyst experimentally and supported by DFT calculations and isotope labeling experiments. Firstly, DFT calculations suggested that the deprotonation of R-OH group of the alcohol on both Au $^{(111)}$ and Pt $^{(111)}$ is more likely to react with OH*, adsorbed on the adjacent, than with a free active site, due to 10-fold lower reaction activation barrier. Secondly, isotope labeled experiments with $^{18}O_2$ and $H_2^{18}O_2$ showed, that oxygen from O_2 is not present in the final carboxyl group, but instead oxygen from H_2O. It has to be emphasized, that the reaction did not take place, if there was no O_2 in the gas phase.

Thus, the "behind the scene" reaction of adsorbed oxygen and water on the metallic NPs seems to be detrimental for the successful oxidation of carbohydrates. It is well known that Au itself is less likely to split O_2 molecule to atoms [8,9], while O* is omnipresent on Pt. Adsorbed O_2 can react with adsorbed H_2O [6,7] to form OOH* and OH*. The former can degrade to O* and OH*, which is again, according to DFT, more likely to occur on Pt $^{(111)}$, than on Au $^{(111)}$ (*Ea* of 52 and 83 kJ mol^{-1}, respectively). Also, OOH* can react with water, forming peroxide and an additional OH*. Peroxide can degrade to two OH*, and similarly as above, this reaction is more likely to occur on Pt $^{(111)}$ than on Au $^{(111)}$ (Ea of 29 and 71 kJ mol^{-1}, respectively). In short, the studies above suggest, that base-free SO of alcohols and aldehydes will occur, if OH* is present on the surface. Catalysts, with Au as the active metal, often requires the addition of a base for the reaction to occur [6,7,10–12], while Pt catalysts do not [6,13–15]. The problem associated with Au based catalysts are usually the low productivity, while for Pt, the high productivity is often limited by overoxidation and metal leaching.

Contrary to monometallic, bimetallic catalysts seem to have the best from both worlds – high productivity and stability. Numerous studies report the SO ability of bimetallic AuPt catalysts in base-free conditions [9,16–18]. However, there is only a handful of studies, describing the SO kinetics of glucose (GLC) to glucaric acid (GA). The first step, oxidation of GLC to gluconic acid (GU), has been well described, with *Ea* determined from 46 to 50 kJ mol^{-1} and a Langmuir-Hinshelwood mechanism for GLC and O_2 [19–24]. In our previous paper [9], we partially addressed this issue with a kinetic model, which described the reaction pathway relatively good. However, looking closely to the data for the oxidation of xylose to xylaric acid [25] and base free studies for GLC to glucaric acid [9,16] there is a clear distinction in the reaction rates for reactants (sugars), intermediates (aldonic/uronic acids) and products (aldaric acids). First step (sugar to aldonic acid) seems fast, the second step (aldonic to uronic acid) is limitingly slow, and the third step (uronic to aldaric acid) is relatively fast, but not as fast as the first one. This is, however, not surprising due to the fact that the first step is usually the oxidation of the formyl group (if open chain) or alcohol (pyranose), the second step is of the primary alcohol and the third step, again, of the formyl group. For example, oxidation of GLC and glucuronic acid (GLU) was studied by Klis et al. [26] on Au/TiO_2 catalyst in a base-free conditions, and the results showed, that GLU conversion rate is slower, and requires higher temperature to reach the same conversion. Our previous investigation showed that Au/ZrO_2 also converts GLC to GU in a base-free conditions, but further oxidation to GLU and GA is very slow. Additionally, from previous studies [9,16,25] it can be distinguished that once a certain amount of aldaric acid is formed, all reactions are slowed down, pointing to the fact that aldaric acids, once formed, reversibly block the active sites. Finally, it has to be emphasized, that direct comparison of previous studies is a tedious task, since different supporting materials, catalyst synthesis procedures and process conditions were applied.

There is a clear need to study the selective oxidation of sugars with heterogeneous catalysts, to accurately determine the rate limiting steps and provide new aspects of the unique reaction mechanism phenomena. For the reasons mentioned above, the aim of this study was to perform a set of experiments (25 experiments, 700 concentration points) with AuPt/ZrO_2 catalyst in base - free conditions, with GLC, both intermediates (GU and GLU) and GA at different temperatures, O_2 pressures and starting reactant concentrations and to build a comprehensive kinetic model, encompassing all tested experimental variables, with additional validation experiments.

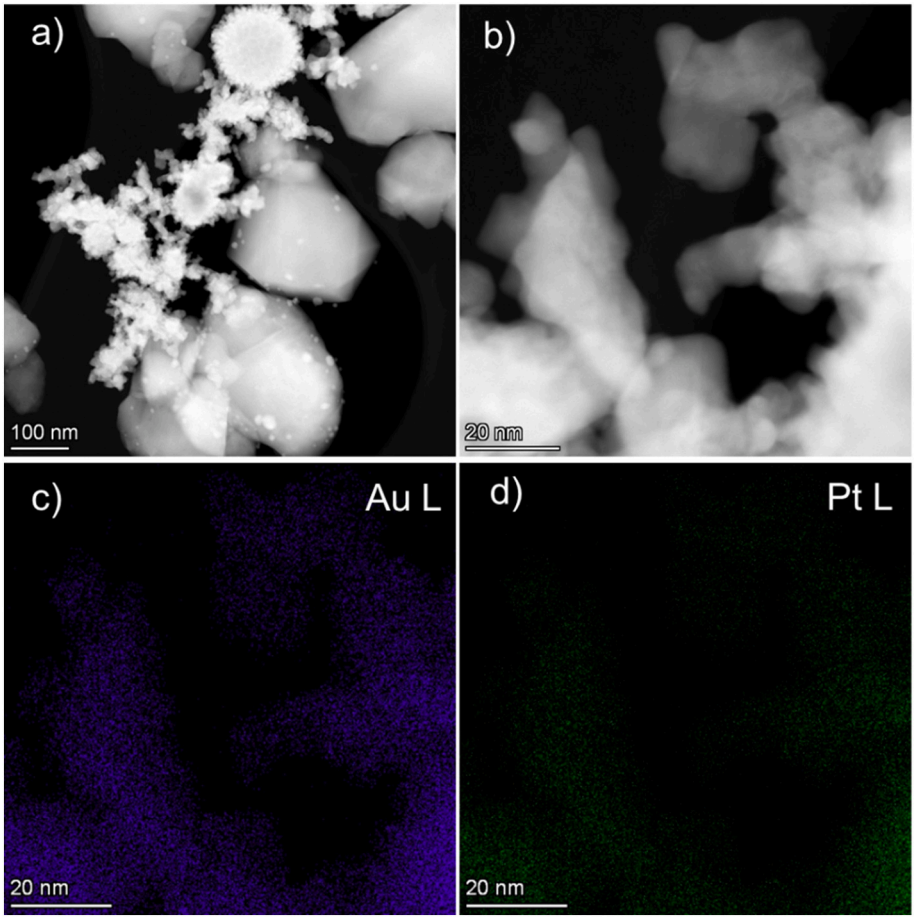

Fig. 3. High-angle annular dark field STEM images of the AuPt 67:33 catalyst a) and b) and the corresponding elemental maps c) and d) of AuPt agglomerate imaged in b).

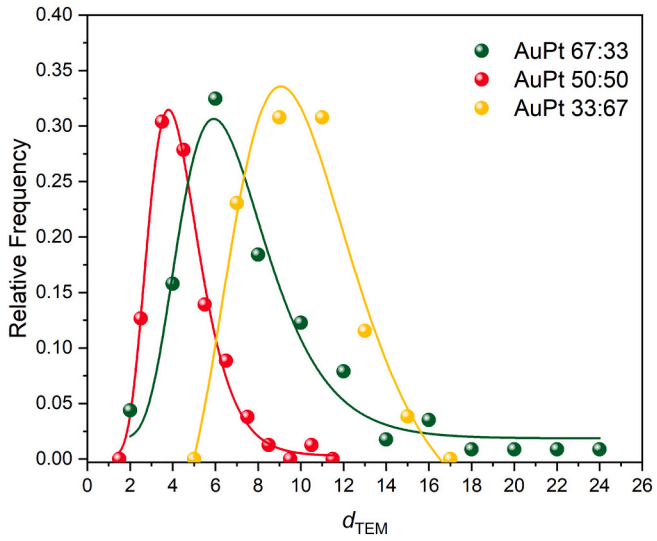

Fig. 4. Empirical size distributions (dots) fitted with a log-normal distribution functions (curves) for the AuPt NP.

2. Materials and methods

2.1. Catalyst synthesis

Catalyst synthesis procedure was performed in the following manner: firstly, 4 g of ZrO_2 support was dispersed in 80 mL of deionized water (dH_2O) with a resistivity of 18.2 MΩ. Different ratios of $HAuCl_4$ x H_2O and $PtCl_4$ were dissolved separately in 10 mL dH_2O to achieve loading of the catalyst with 7 wt% active metals. The metal solution was then added dropwise to the dispersed carrier while stirring vigorously. After 10 min, the pH was adjusted to 8 with a 2.5 vol% aqueous NH_4OH solution. The suspension was stirred for a further 2 h at room temperature. Subsequently, 500 μL hydrazine hydrate (80 % aqueous solution) was added to reduce the metal ions. The resulting catalyst was recovered by centrifugation, the supernatant was discarded, while the catalyst residue was re-dispersed in dH_2O. This washing step was repeated three times to ensure thorough purification of the catalyst. After centrifugation, the catalyst powder was dried overnight in an oven at 80 °C.

2.2. Catalyst characterization

The phase composition of the crystalline samples was analyzed using X-ray powder diffraction (PANalytical X'Pert PRO) at 45 kV with a CuKα1 radiation source. Data were collected over a 10°–90° range with a step size of 0.05° and a counting time of 500 s. The resulting diffractograms were interpreted using the Profex software package (ver. 5.1.0) with crystal structure data from the Crystallography Open Database (COD).

The composition and distribution of AuPt NP on the ZrO_2 particles were analyzed using the Thermo Scientific Talos F200X scanning transmission electron microscope (STEM) and energy dispersive X-ray spectrometer (EDXS). The samples were crushed in an agate mortar, dispersed in isopropanol and dripped onto a C-foil with Cu support and dried at ambient conditions.

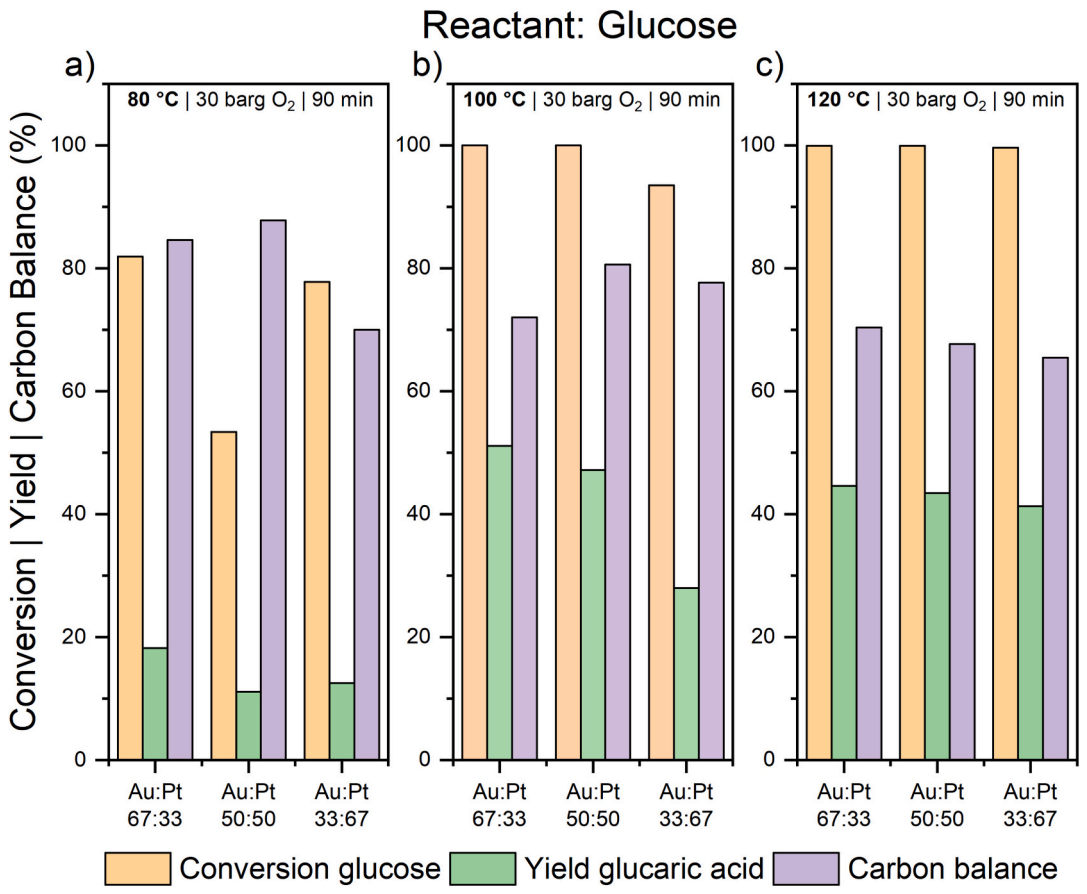

Fig. 5. GLC conversion, GA yield and carbon balance. Experimental conditions: reaction time of 90 min, GLC concentration of 0.025 M, reaction temperature of 80 (a), 100 (b) and 120 °C (c), and O_2 pressure of 30 barg.

Empirical, number-weighted, particle-size-distribution functions were estimated from the HAADF STEM images. The particle size is given as an equivalent diameter—the diameter of a circle having the same surface area as the imaged particle. The empirical number-weighted distributions were fitted with a log-normal distribution function. The average size (d_{TEM}) and standard deviation (σ_{TEM}) were calculated from known relationships between the arithmetic moments and the parameters of the log-normal distribution function [27].

2.3. Catalytic experiments

The catalytic activity experiments were performed in parallel 75 mL stainless steel batch reactors (Parr 5000 series) equipped with a magnetic stirrer operating at 800 rpm. Each reactor was equipped with a liquid phase sampling line to allow regular sampling during the experiment. The liquid reaction mixture consisted of 40 mL of the reactant (GLC, GU, GLU and GA) at various concentrations and 700 mg of catalyst. Prior to the start of the experiment, each autoclave was purged three times with nitrogen (5.0, Messer, Bad Soden am Taunus, Germany), followed by a subsequent pressurization with oxygen in the range of 1 to 30 O_2 barg (gauge pressure). Experiments were performed at 3 different temperatures (80, 100 and 120 °C) and two different reactant concentrations (0.025 and 0.25 M).

2.4. Characterization of spent catalyst

To assess the extent of eventual coking of the catalyst during the oxidation experiment, thermogravimetric analysis (TGA) was conducted using a PerkinElmer Spectrum 3 coupled with an EGA 4000 module. The analysis was performed on both fresh and spent catalysts. The spent catalyst, after the experiment, was separated via centrifugation and dried at 60 °C until a constant mass was reached. Approximately 10 mg of each catalyst sample was subjected to a controlled heating program at a rate of 5 °C min^{-1} from 25 °C to 800 °C under an air atmosphere.

2.5. Liquid phase analysis

High-performance liquid chromatography (HPLC) was used to determine the degree of oxidation of the GLC. The analysis was performed with a Thermo-Fisher Scientific UltiMateTM 3000 UHPLC system equipped with both a diode array detector (DAD) and a refractive index detector (RI). The chromatography column used was the Rezex RHM monosaccharide H^+ column accompanied by a guard column of the same type. The mobile phase consisted of ultrapure water (resistivity: 18.2 MΩ). The temperature of the column was maintained at 60 °C and a flow rate of 0.6 mL min^{-1}. The analytes were detected with the RI detector.

Ion chromatography (IC) was used to quantify GU, GLU, GA, tartaric acid, tartronic acid, glycolic acid, oxalic acid and formic acid. The acidic reaction by-products were analyzed using a Dionex ICS 6000 ion chromatograph equipped with an eluent generator, a suppressor and a conductivity detector. Samples were taken systematically throughout the experiment and stored under refrigeration until they were diluted with MilliQ water, filtered and analyzed. Adequate separation of analytes was achieved using a Dionex IonPac AS11-HC analytical column, 4 × 250 mm, paired with a suitable precolumn (Dionex IonPac AG11-HC, 4 × 50 mm). A potassium hydroxide (KOH) gradient was used, starting with 2 mM for 8 min, followed by a stepwise increase over 25 min to 35 mM KOH (suppressor was set to 130 mA). The injection volume was set to 10 μL, the flow rate to 1.5 mL min^{-1} and the column temperature to 35 °C.

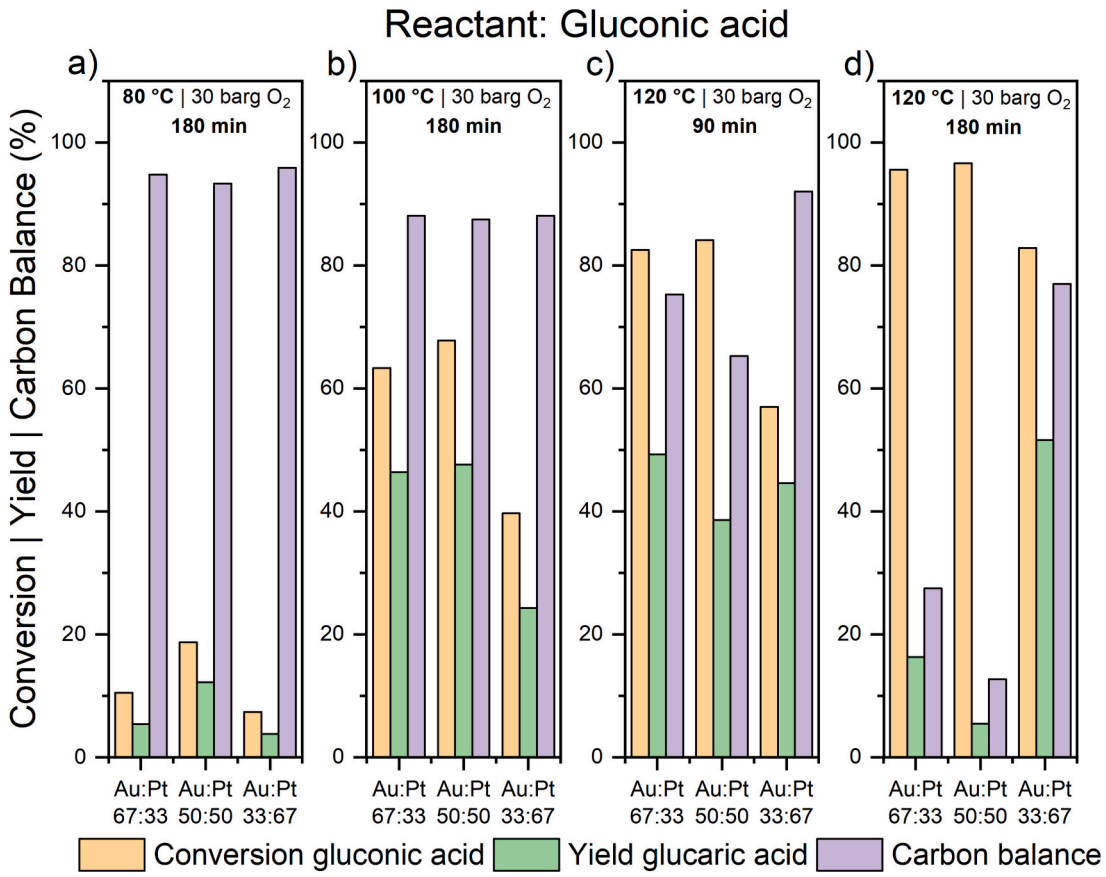

Fig. 6. GU conversion, GA yield and carbon balance. Experimental conditions: reaction time of 90 (c) or 180 (a, b, d) min, GU concentration of 0.025 M, reaction temperature of 80 (a), 100 (b) and 120 °C (c, d) and O_2 pressure of 30 barg.

2.6. Kinetic model

The kinetic model from our previous study [9], has been substantially improved in terms of specific reactions, occurring on the catalyst's active sites. A simplified reaction scheme is shown in Fig. 1, while the exact reaction mechanism with all steps is shown in Fig. S1 and also in Table 1.

Firstly, O_2 solubility (equilibrium concentration of dissolved oxygen) has been determined with Eq. (1), from [28], using oxygen partial pressure and temperature to determine the equilibrium oxygen concentration in the liquid phase.

$$C_{O_2}^{sat} = \frac{55.56 P_{O_2}}{\exp\left(3.71814 + \frac{5596.17}{T} - \frac{1049668}{T^2}\right) - P_{O_2}} \quad (1)$$

Gas-liquid transfer rate was calculated with Eq. (2).

$$r_{O_2}^{G-L} = k_{O_2}^{L} \bullet a_g \bullet \left(C_{O_2}^{sat} - C_{O_2}^{L}\right) \quad (2)$$

Since the exact gas-liquid interphase area in Parr 5000 reactors could not be determined, k^{L}_{O2} and a_g were merged into one constant k_{La} [min^{-1}], as shown in Eq. (3).

$$k_{La} \propto k_{O_2}^{L} \bullet a_g \quad (3)$$

Mass transfer resistance on the gas side was considered negligible due to the use of high-purity oxygen.

The adsorption rate (r_j^{ads}) of each compound j depends on the adsorption rate constant (k_j^{ads}), its concentration in a liquid phase (C_j^{L}) and the concentration of vacant sites (Θ_{vs}), defined in Eq. (4).

$$r_j^{ads} = k_j^{ads} \bullet C_j^{L} \bullet \Theta_{vs} \quad (4)$$

Adsorption rate constants were determined separately, by the regression analysis, for O_2 and all C_6 compounds. Furthermore, the active sites, for oxygen species on the surface (O_2*, OH* and O*), were separated from the active sites for C_6 compounds, based on the bimetallic nature of the catalyst and also experimental evidence. More specifically, the classical treatment of Langmuir- Hinshelwood kinetics on uniform surfaces was extended to reactions occurring on two types of sites in close proximity, both of which are present on the AuPt NP. Similar *quasi equilibrium approximation* mechanism was described by Salmi and Murzin in their book *Catalytic Kinetics* [29].

The dual site assumption in our kinetic model is indirectly backed by previous studies. A study by Zope [30], where Au/TiO_2 and Pt/C catalysts were studied for glycerol oxidation showed that compounds with OH bound to secondary carbon atoms (like sugar acids and polyols) can block the reaction by adsorbing on the surface. They also showed that without a pH control, the reaction does not proceed and in the case of Pt/C, the addition of GLU completely stopped glycerol conversion. This clearly shows that GU acts as an inhibitor when monometallic Au and Pt catalysts are used. On the other hand, Vlachos et al. [31] reported that Pt/C can produce glucaric acid in base-free conditions when starting from GLC or even GU, while Au shows no such activity. Additionally, in a previous study, Dimitratos et al. [32] compared monometallic and bimetallic catalysts under base-free conditions. They showed that monometallic Au did not convert any of the tested alcohols (benzyl alcohol, cinnamyl alcohol and octanol), while bimetallic AuPd and AuPt exhibited significant activity. In fact, AuPd consistently outperformed Pd alone, and AuPt, although not better than Pt, was still much more active than Au by itself. This strongly indicates that Au on its own is inactive in base-free systems, but when combined with another metal it contributes to the presence of new types of active sites. Such results provide indirect but convincing evidence that bimetallic catalysts may

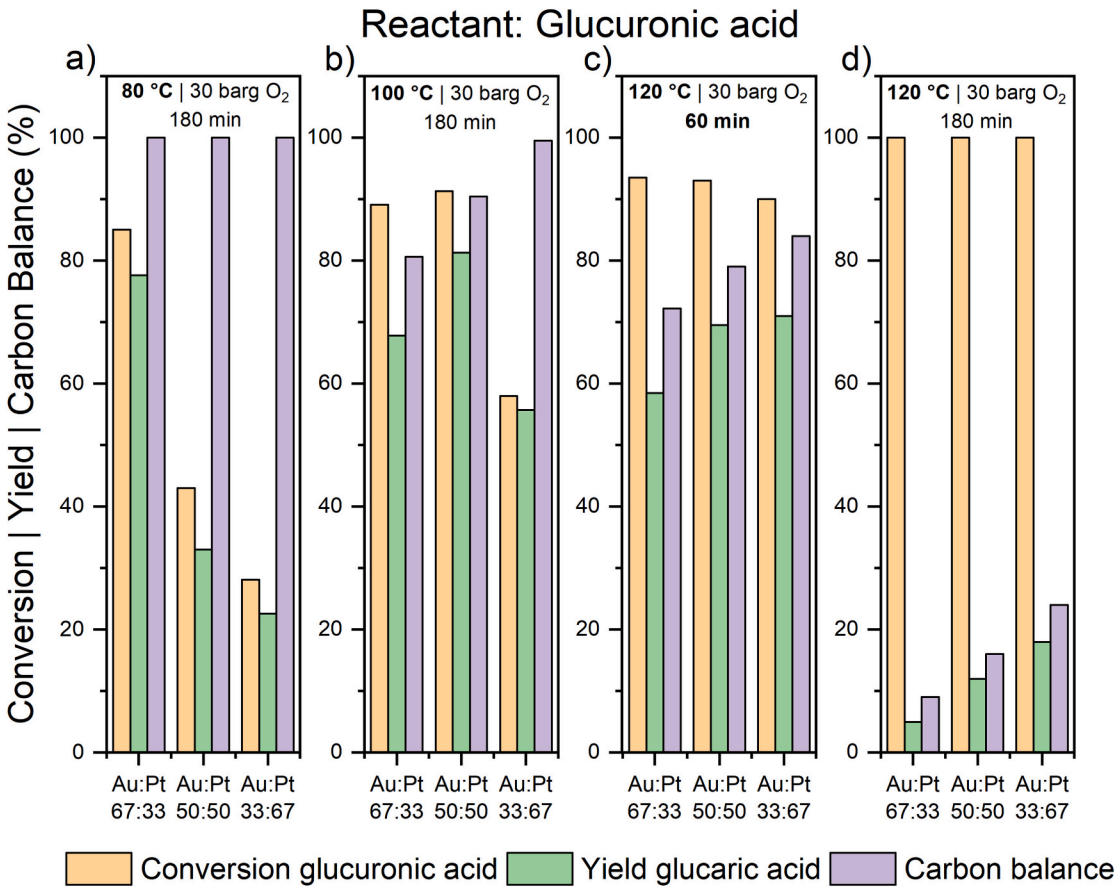

Fig. 7. GLU conversion, GA yield and carbon balance. Experimental conditions: reaction time of 60 (c) or 180 (a, b, d) min, GLU concentration of 0.025 M, reaction temperature of 80 (a), 100 (b) and 120 °C (c, d) and O_2 pressure of 30 barg.

Table 2
Reaction rate constants and activation energies obtained by regression analysis of experimental data (25 exp., 700 exp. points).

Reaction # (*i*)	k_i at 100 °C (min^{-1})	Ea_i (kJ mol^{-1})
1	2978 ± 271	>5
2	5 ± 1	62 ± 12
3	120 ± 2	51 ± 5
4	51 ± 2	59 ± 14
5	15 ± 1	57 ± 10
6	(4 ± 1) · 10^{-2}	56 ± 7
7	(3 ± 1) · 10^{-2}	89 ± 13

Table 3
Adsorption/desorption rate constants obtained by regression analysis of experimental data (25 exp., 700 exp. points).

Adsorption/desorption rate constants (min^{-1})	
k_{ads}	120 ± 2
$k_{des\ GLC}$	(68 ± 8) · 10^3
$k_{des\ GU}$	(25 ± 3) · 10^3
$k_{des\ GLU}$	(10.0 ± 0.2) · 10^3
$k_{des\ GA}$	178 ± 23
$k_{des\ OTHR}$	insignificant
$kO_{2\ ads}$	122 ± 2
$k_{des}O2$	(1.00 ± 0.01) · 10^3

possess different and complementary active sites compared to monometallic gold catalysts.

The total amount of active sites (n_{TS}) was calculated from the mass of the catalyst, used in the experiment (all experiments 700 mg), and the C_{AS} active sites density (233 μmol g^{-1}), determined from oxygen pulse chemisorption in our previous study [9]. The storage capacity of O_2*, O* and OH*, were separated, based on the NP's elemental composition, determined from STEM/EDX, and will be discussed in the results section.

The desorption rate (r_j^{des}) of each compound *j* depends on the desorption rate constant (k_j^{des}) and coverage of *j*, adsorbed on the active sites (Θ_j), defined in Eq. (5).

$$r_j^{des} = k_j^{des} \bullet \Theta_j \tag{5}$$

During the experiment, temperature and pressure data were recorded to calculate thermodynamic properties such as oxygen solubility. The temperature dependence of the surface reaction was modeled using the Arrhenius equation, as shown in Eq. (6):

$$k_i^{surf}(T_2) = k_i^{surf}(T_1) \bullet \exp\left(\frac{Ea_i}{R} \bullet \left(\frac{1}{T_1} - \frac{1}{T_2}\right)\right) \tag{6}$$

The surface reaction rate (r_j^{surf}) of each compound depends on the surface reaction rate constant (k_j^{surf}), the C_6 compound coverage on the catalyst surface (Θ_{C6}) and the concentration of oxygen species on the surface (Θ_X, x = O^{ads}, OH^{ads}) as shown in Eq. (7).

$$r_i^{surf} = k_i^{surf} \bullet \Theta_{C6} \bullet \Theta_X \tag{7}$$

The differential balance equations with respect to the assumed reaction network are as follows (Eqs. (8)–(12)):

The general oxygen balance in the gaseous phase is shown by Eq. (8).

$$\frac{dn_{O_2}^G}{dt} = -r_{O_2}^{G-L} \bullet V_L \tag{8}$$

The general balances of compounds (GLC, GU, GLU, GA and others)

Table 4
Maximum TOF values, determined for each experiment. If the compound was not used in the experiment, its TOF value for corresponding reaction was not present (n. p). **Bolded** TOF values represent the reactions, which include the starting reactant.

Entry	Reactant, concentration, T, p	Corresponds to Figure…	max TOF 1 [min^{-1}]	max TOF 2 [min^{-1}]	max TOF 3 [min^{-1}]	max TOF 4 [min^{-1}]	max TOF 5 [min^{-1}]	max TOF 6 [min^{-1}]	max TOF 7 [min^{-1}]
1	GLC, **0.025 M, 100 °C, 30 barg O_2**	Fig. 10a,Fig. 11a, **S15a**	0.38	0.1339	**0.44**	0.15	0.09	0.016	0.018
2	GU, **0.025 M, 100 °C, 30 barg O_2**	Fig. 10b, Fig. 11b, **S15b**	0.17	0.0336	n.p.	**0.07**	0.04	0.016	0.023
3	GLU, **0.025 M, 100 °C, 30 barg O_2**	Fig. 10c, Fig. 11c, **S15c**	0.18	0.1206	n.p.	n.p.	**0.17**	0.015	0.010
4	**GLC, 0.025 M, 100 °C,** 1 barg O_2	Fig. 9a, **S8a, S14a**	0.01	0.0080	**0.38**	0.10	0.07	0.017	0.021
5	**GLC, 0.025 M,** 120 °C, **1 barg O_2**	Fig. 9b, **S8b, S14b**	0.02	0.0141	**0.59**	0.15	0.13	0.042	0.089
6	**GLC, 0.025 M, 100 °C,** 10 barg O_2	Fig. 9c, **S8c, S14c**	0.11	0.0395	**0.33**	0.12	0.08	0.017	0.020
7	**GLC, 0.025 M, 100 °C,** 20 barg O_2	Fig. 9d, **S8d, S14d**	0.22	0.0684	**0.34**	0.13	0.09	0.018	0.019
8	GLC, 0.25 M, **100 °C, 30 barg O_2**	Fig. 13a, **S10a, S17a**	2.30	0.3408	**2.63**	0.84	0.29	0.026	0.019
9	GU, **0.25 M, 100 °C, 30 barg O_2**	Fig. 13b, **S10b, S17b**	0.18	0.0038	n.p.	**0.09**	0.05	0.022	0.023
10	GLU, **0.25 M, 100 °C, 30 barg O_2**	Fig. 13c, **S10c, S17c**	0.31	0.2289	n.p.	n.p.	**0.38**	0.014	0.005
11	**GLC,** 0.025 M, 80 °C, **30 barg O_2**	Fig. 12a, **S9a, S16a**	0.19	0.0396	**0.17**	0.06	0.04	0.006	0.004
12	**GLC, 0.025 M,** 120 °C, **30 barg O_2**	Fig. 12b, **S9b, S16b**	0.60	0.1691	**0.54**	0.22	0.18	0.040	0.075
13	GU, **0.025 M,** 80 °C, **30 barg O_2**	Fig. 12c, **S9c, S16c**	0.18	0.0020	n.p.	**0.04**	0.01	0.004	0.005
14	**GU, 0.025 M,** 120 °C, **30 barg O_2**	Fig. 12d, **S9d, S16d**	0.20	0.1629	n.p.	**0.12**	0.10	0.037	0.077
15	GLU, **0.025 M,** 80 °C, **30 barg O_2**	Fig. 12e, **S9e, S16e**	0.18	0.0330	n.p.	n.p.	**0.09**	0.004	0.001
16	**GLU, 0.025 M,** 120 °C, **30 barg O_2**	Fig. 12f, **S9f, S16f**	0.19	0.3106	n.p.	n.p.	**0.25**	0.038	0.044
17	GLC, 0.25 M, 80 °C, **30 barg O_2**	**S7a, S11a, S18a**	0.94	0.0947	**1.01**	0.33	0.11	0.009	0.004
18	**GLC, 0.25 M,** 120 °C, **30 barg O_2**	**S7b, S11b, S18b**	3.92	0.4848	**4.06**	1.33	0.59	0.065	0.078
19	GU, **0.25 M,** 80 °C, **30 barg O_2**	**S7c, S11c, S18c**	0.19	0.0004	n.p.	**0.08**	0.01	0.005	0.005
20	**GU, 0.25 M,** 120 °C, **30 barg O_2**	**S7d, S11f, S1d**	0.30	0.0698	n.p.	**0.19**	0.16	0.062	0.095
21	GLU, **0.25 M,** 80 °C, **30 barg O_2**	**S7e, S11e, S18e**	0.28	0.0557	n.p.	n.p.	**0.30**	0.002	0.000
22	**GLU, 0.25 M,** 120 °C, **30 barg O_2**	**S7f, S11f, S18f**	0.60	0.6737	n.p.	n.p.	**0.80**	0.048	0.039
23	GU, + GLU 0.025 **M, 100 °C, 30 barg O_2**	Fig. 14a, **S12a, S19a**	0.22	0.0426	n.p.	**0.08**	**0.23**	0.020	0.015
24	GLC + GLU, **0.025 M, 100 °C, 30 barg O_2**	Fig. 14b, **S12b, S19b**	0.41	0.2063	**0.27**	0.09	**0.25**	0.020	0.014
25	GLC + GA, **0.025 M, 100 °C, 30 barg O_2**	Fig. 14c, **S12c, S19c**	0.17	0.0901	**0.14**	0.03	0.03	**0.021**	0.016

in the liquid phase are calculated by Eq. (9), where V_L is the volume of the liquid phase.

$$\frac{dC_j^L}{dt} = -r_j^{ads} + r_j^{des} \bullet \frac{n_{AS\ c6}}{V_L} \quad (9)$$

The general oxygen balance in the liquid phase is calculated by Eq. (10).

$$\frac{dC_{O_2}^L}{dt} = r_{O_2}^{G-L} - r_j^{ads} + r_j^{des} \bullet \frac{n_{AS\ oxygen}}{V_L} \quad (10)$$

The general balances of carbohydrate compounds (GLC*, GU*, GLU*, GA* and others) for active site coverage is calculated by Eq. (11).

$$\frac{d\Theta_j}{dt} = r_j^{ads} \bullet \frac{V_L}{n_{AS\ c6}} - r_j^{des} \pm \Sigma_j^n r_j^{surf} \quad (11)$$

The general balances of oxygen species (O_2*, OH*, O*) for active site coverage is calculated by Eq. (12).

$$\frac{d\Theta_j}{dt} = r_j^{ads} \bullet \frac{V_L}{n_{AS\ oxygen}} - r_j^{des} \pm \Sigma_j^n r_j^{surf} \quad (12)$$

The general balance of carbohydrate compounds (GLC*, GU*, GLU*, GA* and others) for vacant sites is calculated by Eq. (13).

$$\frac{d\Theta_{vs}}{dt} = -\Sigma_j^n r_j^{ads} \bullet \frac{V_L}{n_{AS\ c6}} + \Sigma_j^n r_j^{des} \pm \Sigma_j^n r_j^{surf} \quad (13)$$

The general balance of oxygen species (O_2*, OH*, O*) for vacant sites is calculated by Eq. (14).

$$\frac{d\Theta_{vs}}{dt} = -\Sigma_j^n r_j^{ads} \bullet \frac{V_L}{n_{AS\ oxygen}} + \Sigma_j^n r_j^{des} \pm \Sigma_j^n r_j^{surf} \quad (14)$$

Lastly, turnover frequencies (TOF, min^{-1}) were calculated by Eq. (15).

$$TOF = k_j^{surf} \bullet \Theta_x \bullet \Theta_y \quad (15)$$

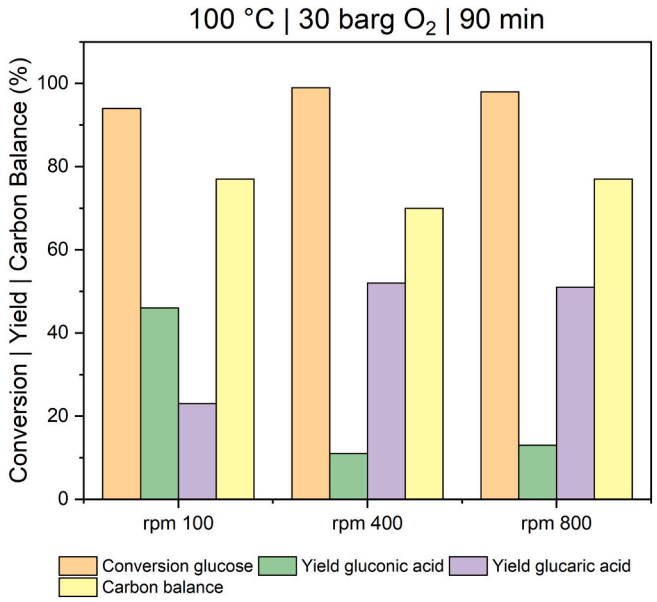

Fig. 8. Different stirring rates, namely 100, 400 and 800 rpm. Experimental conditions: reaction time of 90 min, GLC concentration of 0.025 M, reaction temperature of 100 °C and O_2 pressure of 30 barg.

Matlab 2021b software was used for the numerical analysis of the formulated system. The concentration profiles were solved as a function of time using the *ODE15s* solver. Regression analysis was performed by using *fminsearch* function (Nelder-Mead algorithm). Parameter estimation was performed using the Levenberg – Marquardt algorithm via the *lsqnonlin* function, which also provides the Jacobian matrix. Confidence intervals (CI) were subsequently calculated from the parameter covariance matrix derived from this Jacobian. The initial concentrations of all compounds were set to zero, except for carbohydrate reactant (GLC, GU, GLU or GA) and O_2 (calculated by Eqs. (1)–(3) from initial partial oxygen pressure and temperature of gas mixture at the start of the reaction).

3. Results

3.1. Catalyst characterization

Based on our previous study [9], the crystal structure and phase composition of the synthesized materials were first analyzed by XRD. The only difference, compared to our previous study, was the change in Au:Pt molar ratio, while the total mass of active metal was kept at 7 wt %. When Au is alloyed with Pt, the standard Bragg reflections of fcc Au $^{(111)}$ diffraction peak at 38.1°2θ is not present in the XRD diffractograms of all three catalysts with different Au:Pt molar ratios (Fig. 2). XRD diffractograms suggest that AuPt alloy was formed, since there are no other peaks, which would indicate the deposition of a separate Au or Pt phase. Full XRD diffractograms are shown in Fig. S2.

STEM microscopy was used to analyze the catalysts, in particular to analyze the composition of the AuPt NPs and their distribution over the

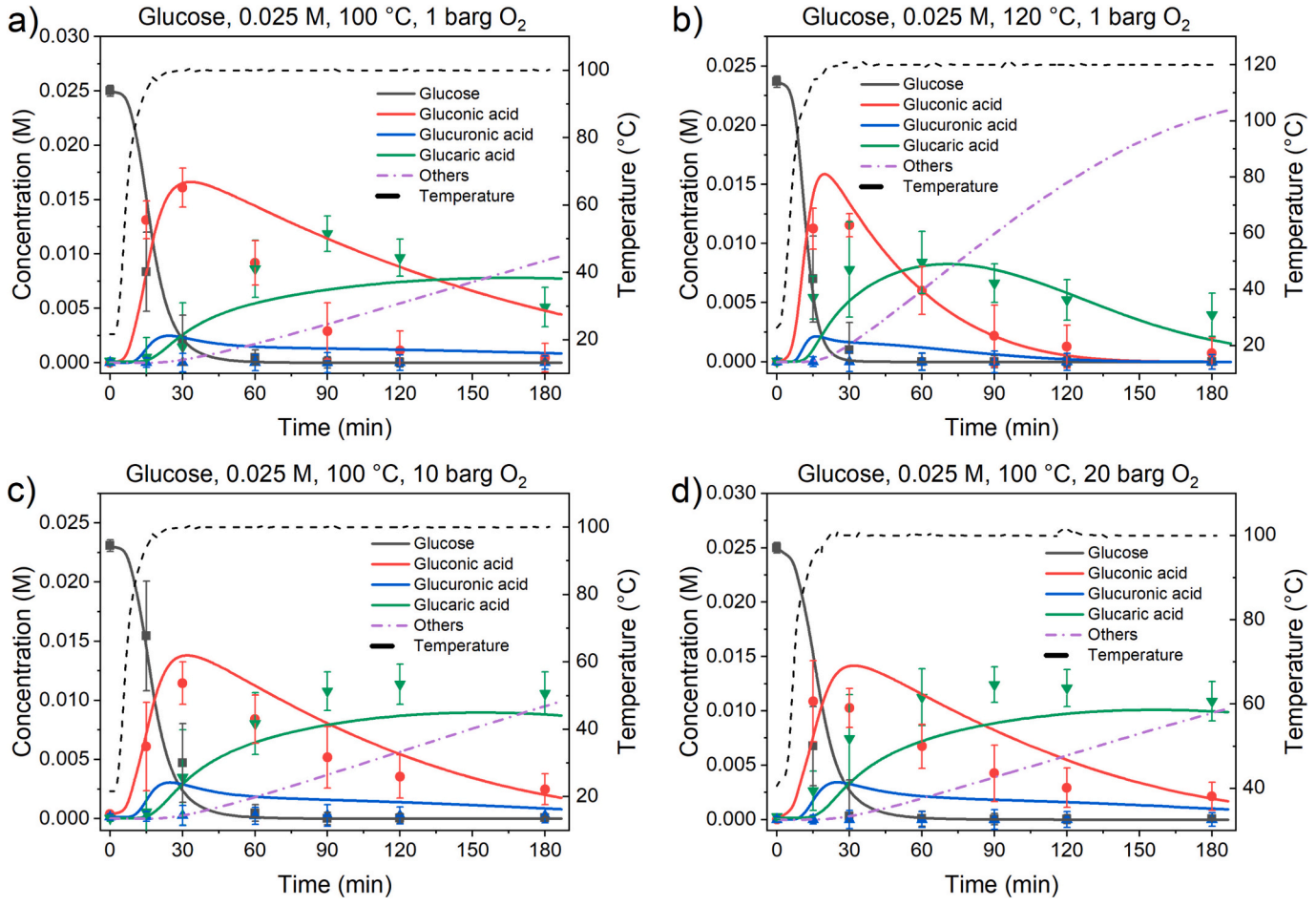

Fig. 9. Experiments (dots) and predicted (lines) concentrations. Experiments at 0.025 M GLC, 100 °C and 1 barg O_2 (a), 120 °C and 1 barg O_2 (b), 100 °C and 10 barg O_2 (c), 100 °C and 20 barg O_2.

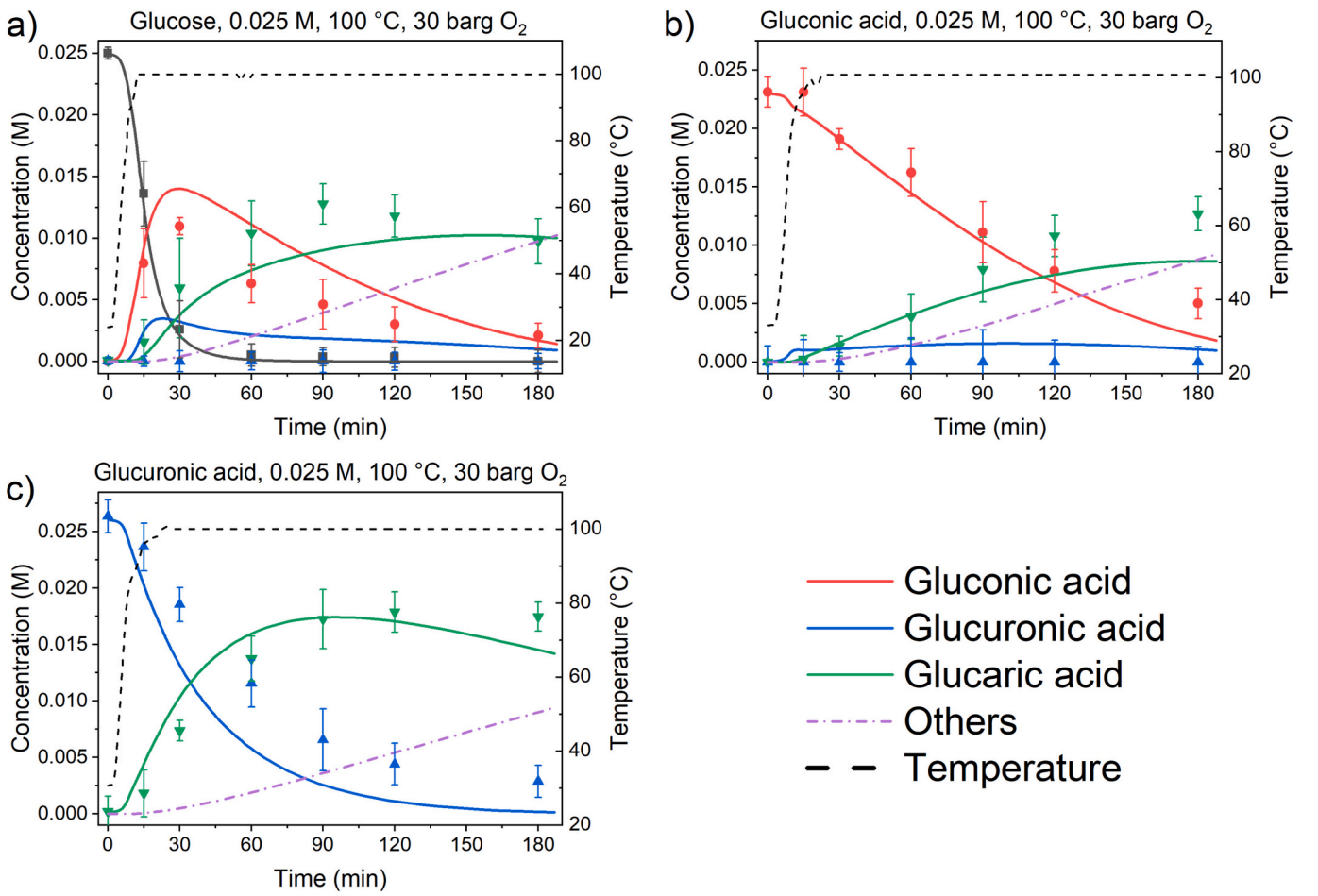

Fig. 10. Experiments (dots) and predicted (lines) concentrations. Experiments at 100 °C, 30 barg O_2 and 0.025 M of GLC (a), GU (b) and GLU (c).

ZrO_2 particles. Fig. 3 shows a typical image of the catalyst particles. The AuPt NPs are present in the form of agglomerates that are relatively homogeneously distributed over larger ZrO_2 particles (100 nm and larger) of undefined shape. The three samples, with different Au:Pt ratios, appeared practically identical.

The homogeneity of the composition of AuPt NPs was verified by EDXS analysis. Several NPs were analyzed and all of them contained both elements (Fig. 3c and d), indicating the formation of an alloy. From this point forward, each catalyst is identified by the nominal molar ratio of Au- to Pt used (e.g., Au:Pt = x:y will be denoted as Au_xPt_y). Similarly, the corresponding figures for $Au_{50}Pt_{50}$ and $Au_{33}Pt_{67}$ are provided in the Supporting Information (Figs. S3 and S4, respectively). However, in all three samples, the AuPt NPs are richer in Au than one would expect, based on the nominal composition, determined at synthesis. For example, the majority of scanned AuPt NPs, for the catalyst material $Au_{67}Pt_{33}$, have composition of 80 % of Au and 20 % of Pt (This trend can be observed at all prepared catalysts, shown in Fig. S5). As it will be shown in the kinetic model section, the number of active sites, available for O_2 adsorption and subsequent conversion to O* and OH*, depends on Au:Pt ratio, determined by EDXS analysis, and not by the nominal ratio determined at synthesis.

Lastly, the AuPt NP distribution of all three synthesized catalysts was determined from STEM images, shown in Fig. 4.

As the figure above depicts, the majority of NP's size is in the range of 2 to 20 nm for all AuPt ratios. However, it can be seen that $Au_{50}Pt_{50}$ exhibits the smallest particle sizes, while the other two ratios produce slightly larger NPs, with $Au_{33}Pt_{67}$ catalyst exhibiting the largest NPs. It has to be mentioned, that NP size-dependent activity experiments have not been studied in this paper, but, as shown in previous studies [23], the size of active metal's NP certainly affects the conversion rate.

3.2. Alloy composition effect on glucaric acid yield

Molar composition of the formed AuPt NPs and its influence on the GLC conversion and GA yield has been reported in previous studies [16,25], where the best results were obtained at Au:Pt molar ratio of 50:50. In our previous paper, the same molar ratio (Au:Pt = 50:50) was used to prepare AuPt/ZrO_2 for the general comparison among monometallic and bimetallic catalysts. However, compared to the study by Derrien [16], the reducing agent was not $NaBH_4$, but hydrazine hydrate. For this reason, catalysts with different Au:Pt ratios were synthesized, to check, whether there are any deviations caused by the synthesis procedure. Fig. 5 represents GLC conversion, GA yield and carbon balance (CB), at different temperatures and pressures.

The highest GA yield at 100 °C is achieved with $Au_{67}Pt_{33}$ catalyst. GA yield is slightly lower with $Au_{50}Pt_{50}$, while with $Au_{33}Pt_{67}$, the lowest amount of GA was produced. GLC conversion at 80 °C for $Au_{50}Pt_{50}$ is surprisingly low, indicating a non-linear relationship for bimetallic composition ratio and conversion at the lower temperature. Additionally, experiments at 120 °C, the conversions, yields and carbon balances are very similar.

When the starting reactant was switched to GU, as shown in Fig. 6, conversions and GA yields are slightly different.

The second reaction step, the oxidation of GU, requires higher temperature to achieve a reasonable conversion. Again, higher GU conversions and GA yields were achieved with $Au_{67}Pt_{33}$ and $Au_{50}Pt_{50}$ catalysts, than with $Au_{33}Pt_{67}$ catalyst. However, at higher reaction temperatures and longer reaction times (Fig. 6d), more GA is preserved on $Au_{33}Pt_{67}$

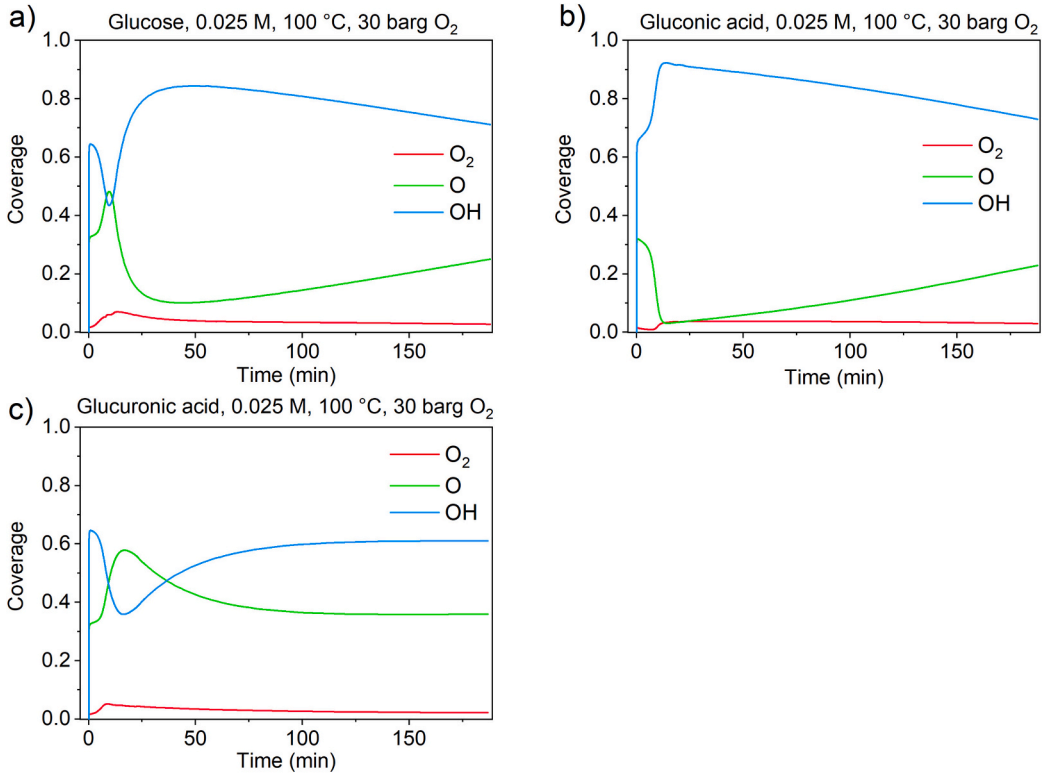

Fig. 11. Predicted oxygen species coverages on active sites, dedicated for oxygen species. Experiments at 100 °C, 30 barg O_2 and 0.025 M of GLC (a), GU (b) and GLU (c).

catalyst, while both $Au_{67}Pt_{33}$ and $Au_{50}Pt_{50}$ decompose GA faster to by-products and eventually CO_2. Lastly, GLU conversion was also compared among the three catalysts. The trend is similar as in Fig. 5, where the highest GLU conversion was achieved with $Au_{67}Pt_{33}$, followed by $Au_{50}Pt_{50}$ and $Au_{33}Pt_{67}$. Surprisingly, at 80 °C, $Au_{67}Pt_{33}$ exceeds in GLU conversion (85 %) and GA yield (77 %), compared to the other two catalysts by a large margin (Fig. 7a). Evidently, the last step from GLU to GA is much more pronounced with $Au_{67}Pt_{33}$.

Similarly, as in Fig. 6, the highest amount of GA was preserved with $Au_{33}Pt_{67}$ at temperature of 120 °C. Additionally, at 100 and 120 °C, and at the reaction time of 60 and 180 min, carbon balance for $Au_{67}Pt_{33}$ is lower compared to the other two catalysts.

Since $Au_{67}Pt_{33}$ catalyst had the highest conversion for both GLC and GLU and the difference between yields for GU was minimal, further experiments, required to construct the kinetic model were performed only with $Au_{67}Pt_{33}$ catalyst.

3.3. Kinetic study

Selective oxidation of GLC to GA is a complex reaction, where consecutive reactions of C_6 molecules react with oxygen species on the catalyst's active sites. Each reaction step with its corresponding reaction rate equation is presented in Table 1.

Reaction 1, between adsorbed O_2* and H_2O*, which produces OH* and O*, was adopted from [5]. The 2nd reaction of O* and H_2O*, which forms OH*, was also included, based on the study of Mom et al. [33]. Reaction 7 is the corresponding backward reaction. For simplicity, water coverage was not included in the kinetic expression, because water is a solvent molecule and is present in excessive amount. Additionally, peroxide formation and its coverage was not included, since the amount of peroxide was considered low, due to its unstable nature. This is corroborated by previous studies, where the amount of detected peroxide was below detection limit when gold was alloyed with Pd [34,35]. A few years later, a DFT study by the same research group revealed, that Pt and Pd have substantially lower activation barrier for peroxide decomposition [6]. Thus, our model assumes that this composition is much faster, relative to all other reactions.

Reactions 3–5 represent main reaction steps from GLC to GA, and were designed accordingly to our previous DFT calculations [9]. In fact, each reaction step, for e.g. from GLC to GU, is a two – step reaction, with a deprotonated intermediate, which cannot be measured analytically. For the sake of simplicity and also to avoid possible over-parameterization, the intermediates were not included in the mass balance equations. For every *two – step* reaction, it was assumed, that one step is much slower than the other one. Therefore, only the limiting step is kinetically relevant and each C_6 specie on the surface reacts with one of the oxygen species. The main difference in the reaction mechanism is that GLC and GLU react with OH*, while GU reacts with O*. This decision was drawn because there is no study, where monometallic Au in base-free conditions produced substantial amount of either GLU or GA. Moreover, in our previous investigation, monometallic Au produced GU from GLC in base-free conditions, and GA was always present in traces. Similar observation was also made by Cao [36] where GA was reported only in traces, when GLC oxidation was performed by Au/TiO_2. This suggests, that Au can also form O* required for the transformation, but, as mentioned earlier, the activation barrier is substantially higher than for Pt, and thus, the reaction rate is lower.

Reaction 6 represents the decomposition of GA to smaller by products, e.g. tartaric, tartronic, oxalic, glycolic and formic acid, which were also quantitatively determined with ionic chromatography (IC), but their concentration was much lower and actually, they did not accumulate in the reaction mixture. Thus, it was assumed, that a complete mineralization of all smaller products to CO_2 took place during the experiment. This was also reported in a previous publication by Chaudhari et al. [17], where CO_2 was determined in the gas phase, after the reaction.

To obtain the kinetic parameters with a regression analysis, temperature, pressure and reactant concentration must be varied to obtain

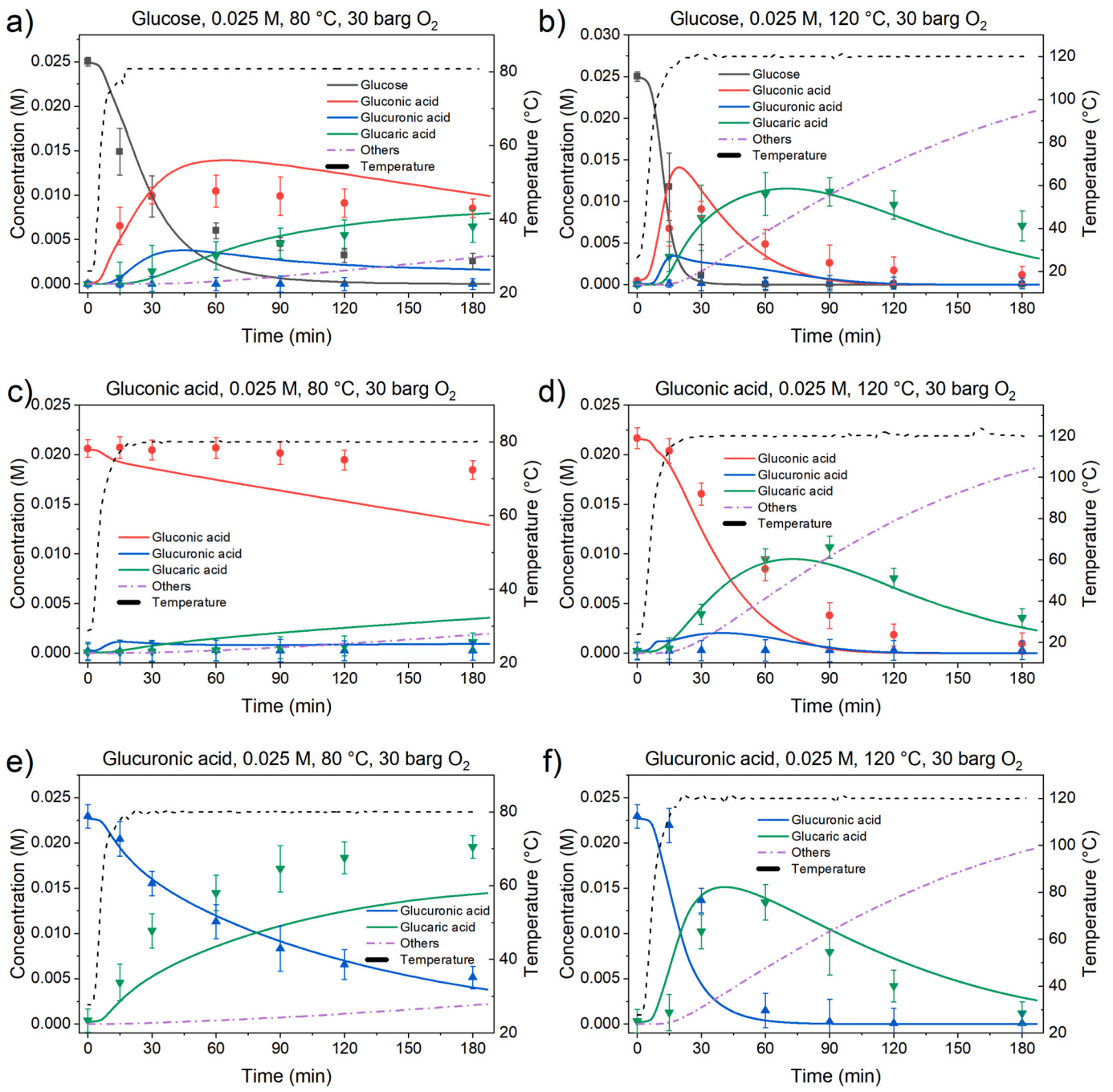

Fig. 12. Experiments (dots) and predicted (lines) concentrations. Experiments at 80 and 120 °C, 30 barg O_2 and 0.025 M of GLC (a, b), GU (c, d) and GLU (e, f).

the concentration-time profiles over a wide range of process conditions. Also, experiments with intermediates, such as GU and GLU have to be performed, to isolate all consecutive reactions, towards the final product. There are also some differences in the adsorption strength among C_6 molecules, since they have different amount of hydroxyl, formyl and carboxyl functional groups [37]. For this reason, 25 experiments with three different reactants, reactant concentrations and reaction temperatures and pressures were performed, producing 700 experimentally determined concentrations points through time, with which the kinetic regression was performed (shown in Table 4, with corresponding maximum TOF values for each reaction step). All relevant kinetic parameters are shown in Table 2 and Table 3.

Because of different desorption rate constants of C_6 species, surface reaction rate constants alone cannot be used to directly compare the reaction rates of all C_6 species. A much better comparison provides a maximum TOF value for each experiment, because it also considers coverages, which differ, precisely because of different adsorption properties of each C_6 specie. In Table 4, maximum TOF values, determined for every experiment, are provided and will be compared to each other, in the following text.

Prior to the start of the experiments, with different temperatures, pressures and reactant concentrations, stirring rate experiments at the same process conditions were performed with GLC as a reactant, to determine the stirring rate, at which gas – liquid mass transfer resistance is eliminated (Fig. 8).

At stirring rate of 100 rpm, the conversion of GLC is 94 %, while at 400 and 800 rpm, GLC conversions are 98 and 99 %, respectively. Furthermore, at 100 rpm, GU and GA yields are 46 and 23 %,

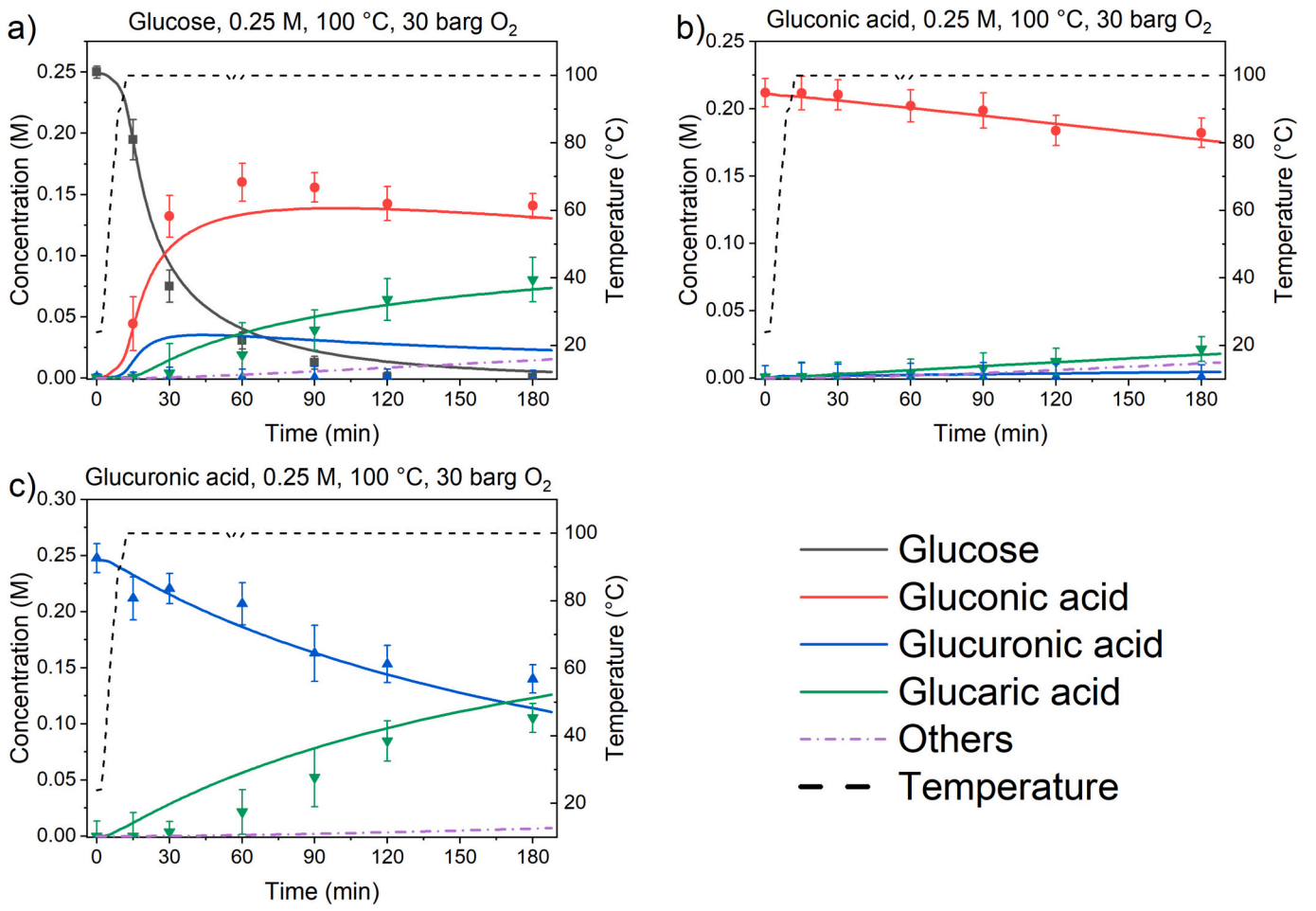

Fig. 13. Experiments (dots) and predicted (lines) concentrations. Experiments at 100 °C, 30 barg O_2 and 0.25 M of GLC (a), GU (b) and GLU (c).

respectively, while at 400 rpm, the yields are 11 and 52 %, which is practically the same as at 800 rpm (GU and GA yields are 13 and 51 %, respectively). This proves that at stirring rates, above 400 rpm, the gas – liquid mass transfer is not the limiting factor anymore. Thus, all further experiments were performed at 800 rpm.

To determine how dissolved oxygen affects the reaction kinetics, a series of tests at 1, 10 and 20 barg O_2 were performed, as shown in Fig. 9.

Results herein suggest that oxygen partial pressure, even at the lowest of 1 barg O_2, does not considerably affect the concentration profile, in terms of all detected products. If C_6 and oxygen species shared the same active sites, all species' conversion would be significantly lower due to the proportional decrease in surface coverage of O_2 at the lowest pressures. However, as shown in Fig. 9a, this is not the case, since at 1 barg O_2, the concentration profiles are practically the same as at higher pressures. Also, an Eley-Rideal mechanism is less probable, since increasing oxygen concentration should, thus, increase the conversion of all species, but it can be seen, that at higher O_2 pressures, concentration profiles remain practically the same. Therefore, the separation of active sites for oxygen and larger C_6 molecules, as described in the *experimental section*, seems plausible, but requires a future quantitative analysis.

Similar observation was also made by a previous study [38], where a pressure ranges from 0.2 atm to 20 atm did not affect the selectivity and yield of the reaction. In another study [25], although Pt/C catalyst was used, the oxidation of xylose to xylaric acid was investigated at different O_2 pressures of 2, 6 and 14 barg in a base-free manner. At 2 barg, the conversion of xylose reached about 90 %, with a xylaric acid selectivity of 30 %. Increasing the pressure to 6 barg improved the conversion to 95 % and the selectivity to about 45 %. A further increase to 14 barg led to a slight improvement in selectivity to 50 %, while the conversion remained almost unchanged. This is yet another suggestion, that Langmuir – Hinshelwood mechanism is at play, and that even at the lowest pressures, oxygen will be able to adsorb and react with water, to produce required oxygen species, despite the coverage of C_6 species. From a practical point of view, operating a Parr reactor at this pressure is challenging. More specifically, sampling is particularly difficult since, at 800 rpm stirring rate, the sampling tube may not be fully submerged, allowing gas to escape and stopping the reaction (no oxidant). The decision was drawn to perform all later experiments at 30 barg pressure, to render the results comparable to our previous study [9] and to ensure a high oxygen amount in the gas phase.

Once reliable process conditions, ensuring a kinetic regime, were determined, experiments with GLC, GU and GLU were performed at 30 barg O_2 and at 100 °C. Fig. 10 shows the experimental (dots) and predicted (lines) results.

GLC oxidation is the fastest (Fig. 10a; entry 1, Table 4), followed by GLU (Fig. 10c; entry 3, Table 4) and finally GU (Fig. 10b; entry 2, Table 4). As it can be seen in Table 4, maximum TOF values for each experiment (TOF value for the reaction, in which the starting reactant was involved) correspond to this trend; 0.44 min^{-1} (TOF_3, starting reactant: GLC), 0.17 min^{-1} (TOF_5, starting reactant: GLU) and 0.07 min^{-1} (TOF_4, starting reactant: GU). As mentioned before, if one were to look only at the reaction rate constants, this trend would not correspond to visual results in Fig. 10, because desorption rate constants are different.

The data also suggests peculiar oxidation of GLU to GA. When GLU is not the starting reactant, its concentration in bulk liquid phase is practically zero, suggesting a fast reabsorption and subsequent reaction to GA. TOF_5 value for experiments in Fig. 10a and b are 0.09 min^{-1} and

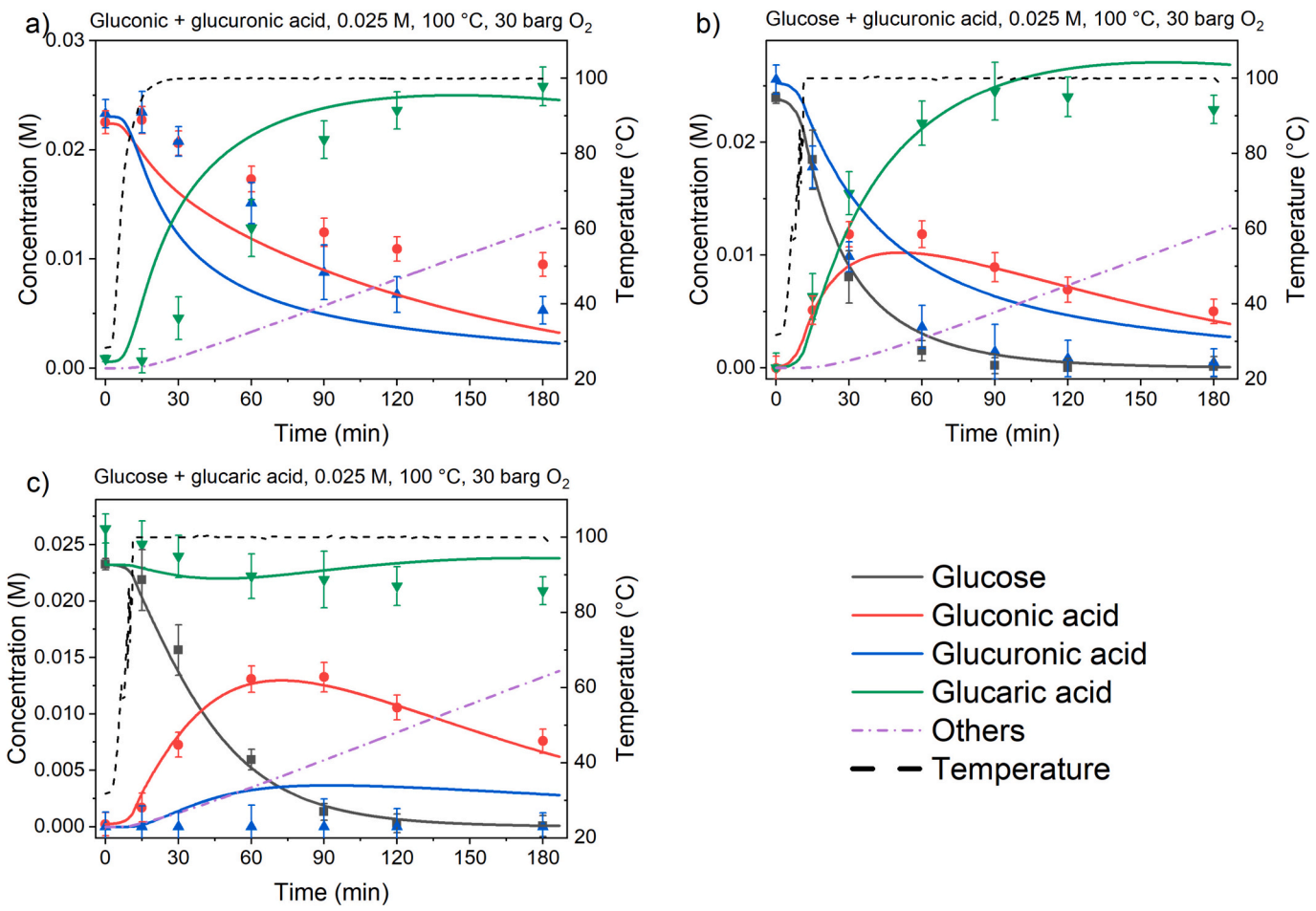

Fig. 14. Experiments (dots) and predicted (lines) concentrations. Experiments at 100 °C, 30 barg O_2 and 0.025 M of GU + GLU (a), GLC + GLU (b) and GLC + GA (c).

0.04 min^{-1}, respectively, which is lower than when GLU is the starting reactant (Fig. 10c, 0.17 min^{-1}).

The difference in dehydrogenation rates of GLC and GLU were already shown by Klis et al. [26], where GLC and GLU were selectively oxidized with Au/TiO_2 in a base-free environment. Our hypothesis is that GLC oxidation occurs with the deprotonation of an alcohol group on C_1 of a pyranose (ring form), and not in an acyclic form, while GLU oxidation can occur in at least two different ways. Firstly, if the oxidation of an aldehyde is considered (formyl group), then the geminal diol should form and subsequently dehydrogenate on the surface to a carboxylic acid. However, it is also possible that GLU in an aldehyde form (direct product from GU oxidation) could transform in the following manner: opening of the ring on C_1 would produce a -COOH, and then the aldehyde group (C_6) would react with the OH group of C_5 to form a lactone. The latter would then react similarly towards GA, as GLC does towards GU. A future NMR or isotope labeling experiment are required, but such experiments are tricky, since sugars and sugar acids with more than 4-carbon atoms are in equilibrium with their lactones in aqueous solutions. Therefore, it would be hard to distinguish if ^{18}O was incorporated during the geminal diol formation or, simply, during the ring opening/closing reactions in the bulk phase.

Another mechanistic distinction is the oxidation of GLC and GU, which can be explained by comparing the hydrogen atom in OH group of GLC on C_1 and hydrogen atom in OH group of C_6. The hydrogen bond of the former is weaker, albeit because of the electron withdrawing effect of the ring oxygen (ether bond). This is observed when comparing reaction rate constants k_3 and k_4 of the kinetic model, where the former is 2.4-fold higher at 100 °C, but in both instances, OH group is believed to be deprotonated.

Detrimental to the final yield of GA is also TOF_6, which is 0.15–0.16 min^{-1} in all three experiments in Fig. 10. In other words, the decomposition rate of GA is relatively constant, regardless of the starting reactant. Additionally, $k_{des\ GA}$, determined by regression analysis, is the lowest (178 min^{-1}, Table 2) among C_6 species, which suggests, that once GA is formed, it adsorbs to the active sites and decomposes to shorter C-species. A DFT study by Monti [37], showed that GA adsorbs much more strongly to the active sites on Au, than GLC and GU, probably due to an additional carboxyl group, which is in line with our model prediction. GA coverage of each experiment can be seen in the *supplementary* part of this paper. Additionally, a TG-MS analysis with fresh and spent catalyst (GLC, 0.025 M, 100 °C, 30 barg O_2) has been performed, to confirm or disprove active site inhibition by irreversible adsorption (coking). Fig. S6 shows that there is practically no difference between fresh and spent catalysts, suggesting that GA inhibition is reversible, and catalyst can be reused multiple times, which was also confirmed by other studies [9,16]. The possibility of humin formation was also excluded, based on a prior study by Armstrong et al. [39].

As mentioned previously, another important aspect of this kinetic model is that GLC and GLU react with OH*, while GU reacts with O*. Due to reactions 1, 2, 7 the coverage of OH* is much higher than of O*. This can be seen in Fig. 11 for all three experiments from Fig. 10.

During the reaction, GLC reacts with OH* to form water and the active site is again available for O_2 adsorption, which further reacts with water to form two new OH* and one O*. When GU is the starting reactant, the coverage of O* is much lower, which subsequently lowers its conversion rate. The exchange between oxygen species dictates the TOF of each C_6 specie. From Fig. 11a, it can be seen that until GLC is present in the reaction mixture (first 30 min of reaction), there is similar

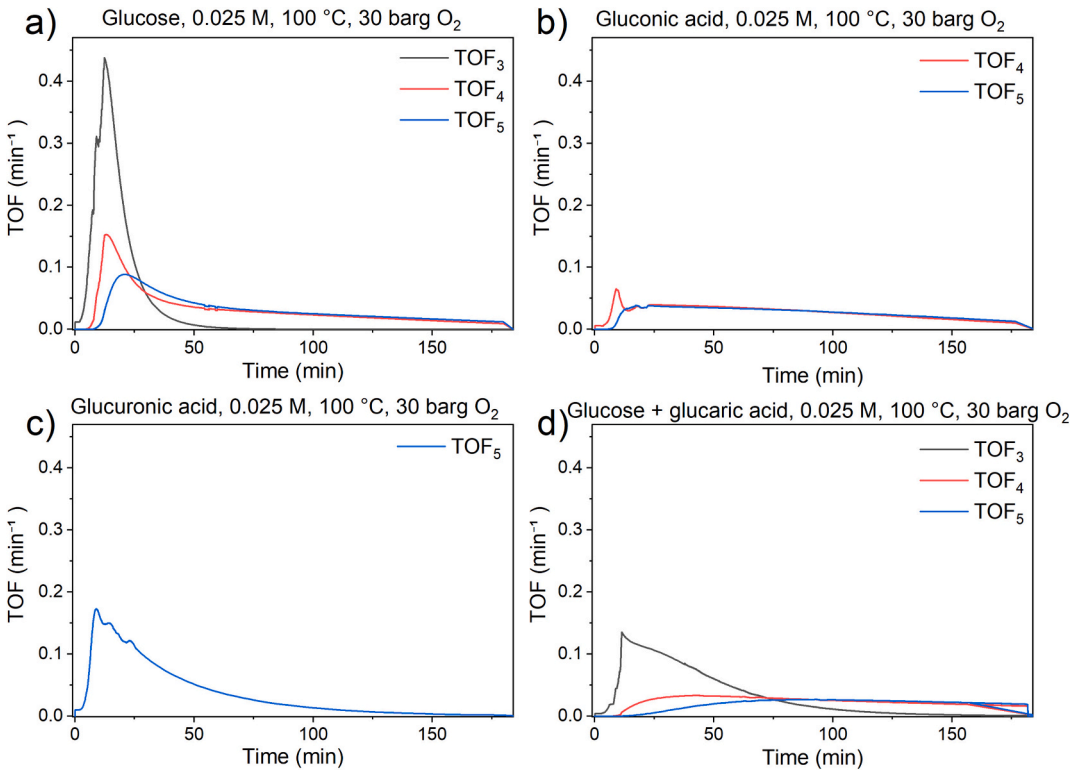

Fig. 15. TOF values throughout the experiment. Experiments at 100 °C, 30 barg O_2 and 0.025 M of GLC (a), GU (b), GLU (c), 0.025 M of GLC + GA (d).

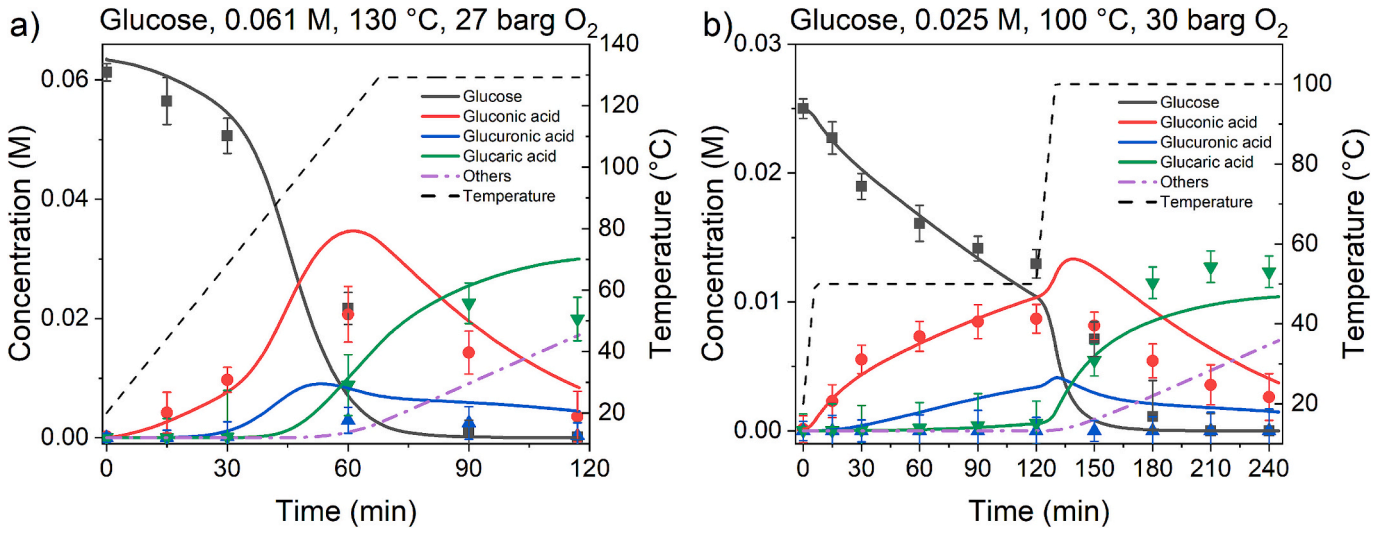

Fig. 16. Experiments (dots) and predicted (lines) concentrations. Experiment was performed at a) 50 for 120 min and at 100 °C for 120 min at 30 barg O_2 and 0.025 M of GLC, b) 130 °C, 117 min at 27 barg O_2 and 0.063 M of GLC with heating rate of 1.6 K min^{-1}.

amount of O* and OH* species on the surface, so the formation of GLU and GA is relatively faster, than after GLC is consumed. TOF values corroborate this observation. When GLC is the reactant (entry 1, Table 4), TOF_4 is 0.15 min^{-1}, while when GU is the reactant at the same process conditions, TOF_4 is 0.07 min^{-1}, meaning that GLC presence affects the oxidation rate of GU.

To provide enough data to calculate the activation energies (Ea's), experiments at 80 and 120 °C were performed with all three reactants (Fig. 12).

At lower and higher reaction temperatures, the concentration profile of each intermediate follows the same trend as at 100 °C. At 80 °C, the conversion rate of all species is slower, even the decomposition of GA. For this reason, the highest GA yield of 85 % was reported for experiment in Fig. 12e, where GLU is the reactant. Contrary, oxidation of GU is much slower at 80 °C. The first reason is that Ea_4 is 59 kJ mol^{-1}, while Ea_3 and Ea_5 are 51 and 57 kJ mol^{-1}, respectively. But this marginal difference of the activation energy is not the only reason for much slower reaction. Activation energy of reaction 7, which produces O* from OH* has a value of 89 kJ mol^{-1}, suggesting, that at lower temperatures, the coverage of O* is even lower than at 100 °C, which is aligned with the study by Mom [33]. This can be observed when comparing Fig. 11 and Fig. S9. On the other hand, at 120 °C, the coverage of O* is much higher, promoting oxidation of GU, which is visible in Fig. 12d. But because the decomposition of GA to smaller

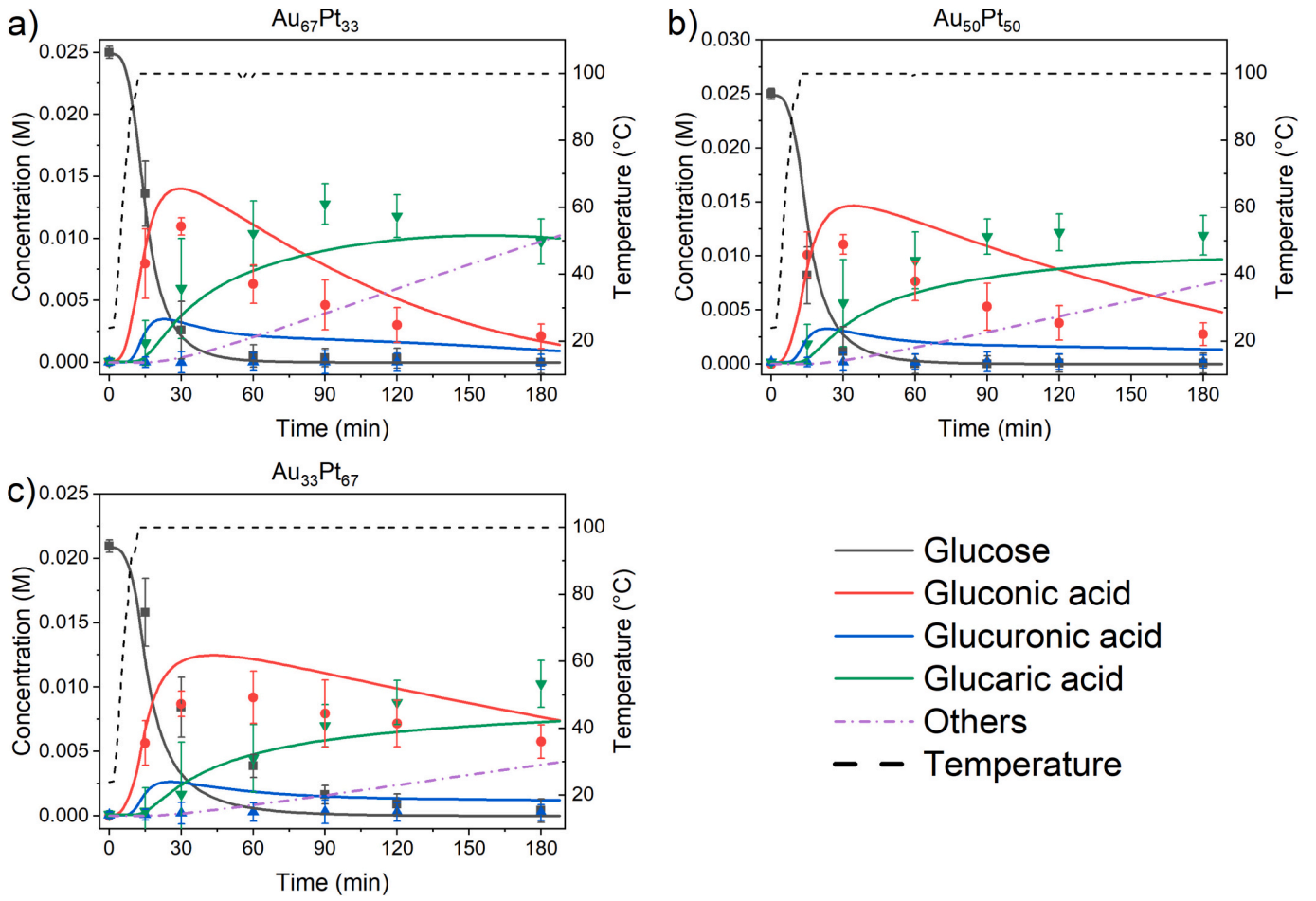

Fig. 17. Experiments (dots) and predicted (lines) concentrations. Experiments at 100 °C, 30 barg O_2 and 0.025 M of $Au_{67}Pt_{33}$ (a), $Au_{50}Pt_{50}$ (b) and $Au_{33}Pt_{67}$ (c).

byproducts (e.g. tartaric, glycolic, tartronic, oxalic and formic acid and eventually CO_2) is also faster at 120 °C, the final GA yield is lower.

Experiments at higher concentrations show different C_6 concentration distribution profiles. The results at 100 °C are shown in Fig. 13.

At higher reactant concentrations (10 – fold), the reaction rate does not scale proportionally, indicating a decrease in available active sites (the amount of the catalyst is the same as in experiments with lower concentrations), likely due to product inhibition effects. When comparing TOF values between experiments at lower (entry 1, 2 and 3, Table 4) and higher (entry 8, 9 and 10, Table 4) concentrations, it can be seen, that while the reactant concentration is 10-fold higher, TOF_3, TOF_4 and TOF_5 values are 6.0, 1.3 and 2.2- fold higher, respectively. Because GA's desorption rate is slower, more active sites are blocked and also, more GA is decomposed to byproducts. The same trend with lower GA yields for "higher concentration experiments" is also observed at 80 and 120 °C, and can be observed in Fig. S7. The corresponding predicted oxygen species coverages on active sites for experiments in Fig. 13 are presented in Fig. S10 and S11.

3.4. Two reactant experiments

As shown in previous sections, with experimental and predicted values, the desorption rates and maximum TOF values differ for GLC, GU, GLU and GA. Especially GA has the lowest desorption rate constant among the latter, which suggests blocking of the active sites for other reacting molecules, which was already reported [37]. For this reason, three more experiments were performed, where 2 reactants were present in the liquid phase at the beginning of the experiment (Fig. 14).

In Fig. 14a, where GU and GLU are reactants, their concentration profiles show a slower conversion rate for both species and also the final concentrations, after 180 min of reaction, of GU and GLU are higher. Regarding TOF values (Entry 23, Table 4), TOF_5 is 0.23 min^{-1}, which is higher than when only GLU is the reactant at the same process conditions (0.17 min^{-1}, entry 3, Table 4). However, the yield of GA is only 56 % (considering both starting reactant's concentrations in the calculation), which is 10 % lower than when GLU is the starting reactant (Fig. 10c), again, suggesting that once GA concentration is high enough, it covers the active sites and decomposes, effectively lowering its final yield.

Similar experiment was performed with GLC and GLU as starting reactants (Fig. 14b, entry 24, Table 4). Interestingly, TOF_3 value was only 0.27 min^{-1}, compared to 0.44 min^{-1} in the experiment with only GLC at the same process conditions (entry 1, Table 4), albeit at the expense of the higher TOF_5 of GLU (0.25 min^{-1}). This is mainly attributed to the fact, that GLU has a lower desorption rate than GLC, but GLC has a higher reaction rate constant.

Lastly, an experiment with GLC and GA was performed, to determine, how higher GA concentrations affect the overall reaction network. Fig. 14c shows, that GA adsorbs and decomposes at a constant TOF_6 value (0.21 min^{-1}). One would intuitively expect that GA's concentration would rise at the beginning of the experiment, but the adsorption of GA lowers all TOF values by a large margin (entry 25, Table 4). TOF_3 is 0.14 min^{-1} instead of 0.44 min^{-1} (entry 1, Table 4), TOF_4 is 0.03 min^{-1} instead of 0.07 min^{-1} (entry 2, Table 4) and TOF_5 is 0.03 min^{-1} instead of 0.17 min^{-1} (entry 3, Table 4). This phenomenon can be observed even better in Fig. 15, where experiments from Fig. 10 (a, b and c) and Fig. 14c are presented with TOF profiles during the reactions.

The maximum value of each peak in Fig. 15 a, b and c are the

corresponding max TOF values from Table 4. When GA is added to GLC at the beginning of the experiment (Fig. 15d), TOF values decrease, because GA adsorbs on the active sites and limits the conversion of all other C_6 compounds.

3.5. Validation experiments

In order to test the model's predictive ability, an experiment with temperature increase during the reaction and an experiment with slower heating rate was performed. For the former, the chosen temperatures were 50 and 100 °C, extrapolating temperature out of experimental framework (T regression range 80–120 °C), while for the latter, the heating rate was set at 1.6 K min^{-1} (heating rate in all other experiments was 5 K min^{-1}). The main ideas were to test the responsiveness of the model to the reaction temperature and to improve the yield of the process with the manipulation of the process parameters.

In the first experiment, where two temperatures were tested, reaction time was set for 120 min for each stage. The algorithm tried to determine the temperature for each stage, while maximizing the final GA yield. The second experiment was performed with proportional weights on reaction time, O_2 partial pressure, and reaction temperature, again maximizing the final GA yield. Fig. 16 shows the results of the predicted concentration profiles, with experimentally determined datapoints.

The prediction and experimental validation depict a reliable prediction of the kinetic model. At temperatures below 70 °C, all reactions rates are slower, with no GA production. Both experiments show that temperature and heating rate can also be extrapolated out of experimental framework and the kinetic model predicts the concentration profiles quite well. Once the temperature is increased, all TOF values rise, forming more GA. Unfortunately, the validation experiments did not improve GA yield, but both cases showed that temperature can be either much lower in the first part of the reaction, and reaction time can be shorter, if slower heating rate and higher target temperature is chosen. In the *supplementary information* part of this paper, the reader is advised to find the coverage of oxygen and C_6 species vs. time of all experiments, presented in this paper for a more in-depth analysis of the kinetic model.

One of the main assumptions of this kinetic model is the separation of active sites into two domains. For the sake of completeness, the AuPt ratio in the model was changed according to the EDXS analysis of the other two catalysts, namely $Au_{50}Pt_{50}$ and $Au_{33}Pt_{67}$, to tests the predictions of the kinetic model. The predictions by the model were compared to experimental data and are shown in Fig. 17.

As it can be seen from the concentration profiles, when the AuPt ratio is changed in the model, the conversion rate is changed. The model suggests that when there fewer active sites available for C_6 compounds, the conversion rate is slower. It should be emphasized that, although the kinetic model reflects the AuPt ratio and predicts its variation quite well, the underlying explanation for this behavior may not be straightforward.

We believe that the reason behind this constraint is that the catalytic performance depends strongly on the balance between the number of Pt atoms and their local electronic/structure environment. Pt is partly responsible for oxygen activation, but when the fraction of Pt in the alloy is too high, the platinum atoms are more likely to sit next to each other. In this case, overoxidation of Pt surface atoms is possible [40], which would effectively reduce the number of active sites available for oxygen activation and thereby slow the overall reaction rate. This results in a lower conversion rate, despite having more Pt present. At the $Au_{67}Pt_{33}$ catalyst, the Pt atoms are most likely available in sufficient numbers to activate oxygen, but they are separated and electronically modified by the gold matrix (or at least more than in the other two catalysts). Gold weakens the binding of oxygen species and prevents surface to become saturated, while platinum ensures that O_2 can still be effectively activated [41]. This balance presumably creates a more favorable reaction environment. However, this simplification requires future ab initio studies and experimental validation.

4. Conclusion

Selective oxidation of carbohydrates is an important field of study, with a lot of yet undiscovered phenomena. In this study, a large experimental database was produced, confirming previous and forming new observations for selective oxidation of glucose to glucaric acid. We report the highest yield of glucaric acid (77 %) from glucuronic acid for a base-free selective oxidation using AuPt/ZrO_2. Furthermore, a detailed kinetic model, encompassing different temperatures, oxygen pressures, reactant concentrations and also reactions with intermediates was developed. The kinetic model predicts quite well the concentration profiles of experiments, with extrapolated process parameters (e.g. lower temperature, than it was used to perform regression to obtain k's and Ea's). It has been experimentally and kinetically proved, that GA's yield, on AuPt/ZrO_2 catalyst, depends on reaction temperature and reactant – to – active metal ratio. Higher reactant (GLC, GU or GLU) concentrations will result in lower GA yields, because when a certain threshold concentration of GA is reached, it will adsorb more strongly to the active sites and decompose. Therefore, future studies should be focused also on the reactor design, with continuous feeding of GLC and removal of GA.

This kind of kinetic model, with oxygen species reactions on the surface, has not yet been reported for the selective oxidation of glucose to glucaric acid. In a broader sense, this study shows how selective oxidation of carbohydrates can be merged with oxygen – water surface reactions, forming reacting species which perform the desired dehydrogenation and formation of aldehydes and carboxylic acids.

CRediT authorship contribution statement

Žan Lavrič: Writing – original draft, Visualization, Validation, Software, Methodology, Investigation, Formal analysis, Conceptualization. **Sašo Gyergyek:** Writing – original draft, Investigation. **Blaž Likozar:** Supervision, Resources, Funding acquisition. **Miha Grilc:** Writing – review & editing, Writing – original draft, Supervision, Software, Methodology, Investigation, Conceptualization.

Declaration of competing interest

The authors declare that they have no known competing financial interests or personal relationships that could have appeared to influence the work reported in this paper.

Acknowledgements

This research was funded by the Slovenian Research and Innovation Agency (ARIS) (research projects N2–0242, GC-0007 and J1–3020 and research core funding P2–0152). S.G. appreciates the funding from the ARIS through program P2-0089 and the access to research equipment via ARIS program P1-0417.

Appendix A. Supplementary data

Supplementary data to this article can be found online at https://doi.org/10.1016/j.cej.2025.170323.

Data availability

Data will be made available on request.

References

[1] K.K. Kapanji, S. Farzad, J.F. Görgens, Life cycle and sustainability assessments of biorefineries producing glucaric acid, sorbitol or levulinic acid annexed to a sugar mill, J. Clean. Prod. 295 (2021) 126339, https://doi.org/10.1016/j.jclepro.2021.126339.

[2] M. Besson, P. Gallezot, C. Pinel, Conversion of biomass into chemicals over metal catalysts, Chem. Rev. 114 (2014) 1827–1870, https://doi.org/10.1021/cr4002269.

[3] J. Teržan, A. Sedminek, Ž. Lavrič, M. Grilc, M. Huš, B. Likozar, Selective oxidation of biomass-derived carbohydrate monomers, Green Chem. 25 (2023) 2220–2240, https://doi.org/10.1039/D2GC04623G.

[4] J.V. Machado, M.L.A. da Silva, C.L.S. Silva, M.C.G. Correia, A.D. da Silva Ruy, L.A. M. Pontes, Catalysts and processes for gluconic and glucaric acids production: a comprehensive review of market and chemical routes, Catal. Commun. 182 (2023) 106740, https://doi.org/10.1016/j.catcom.2023.106740.

[5] S.E. Davis, M.S. Ide, R.J. Davis, Selective oxidation of alcohols and aldehydes over supported metal nanoparticles, Green Chem. 15 (2013) 17–45, https://doi.org/10.1039/C2GC36441G.

[6] B.N. Zope, D.D. Hibbitts, M. Neurock, R.J. Davis, Reactivity of the gold/water interface during selective oxidation catalysis, Science (1979) 330 (2010) 74–78, https://doi.org/10.1126/science.1195055.

[7] S.E. Davis, B.N. Zope, R.J. Davis, On the mechanism of selective oxidation of 5-hydroxymethylfurfural to 2,5-furandicarboxylic acid over supported Pt and Au catalysts, Green Chem. 14 (2012) 143–147, https://doi.org/10.1039/C1GC16074E.

[8] K. Frey, D.J. Schmidt, C. Wolverton, W.F. Schneider, Implications of coverage-dependent O adsorption for catalytic NO oxidation on the late transition metals, Catal. Sci. Technol. 4 (2014) 4356–4365, https://doi.org/10.1039/C4CY00763H.

[9] Ž. Lavrič, J. Teržan, A. Kroflič, J. Zavašnik, J.E. Olszówka, Š. Vajda, M. Huš, M. Grilc, B. Likozar, Selective glucose oxidation to glucaric acid using bimetallic catalysts: Lattice expansion or electronic structure effect? Appl. Catal. B 343 (2024) 123455 https://doi.org/10.1016/j.apcatb.2023.123455.

[10] S. Demirel, M. Lucas, J. Wärnå, T. Salmi, D. Murzin, P. Claus, Reaction kinetics and modelling of the gold catalysed glycerol oxidation, Top. Catal. 44 (2007) 299–305, https://doi.org/10.1007/s11244-007-0303-y.

[11] I. Sobczak, K. Jagodzinska, M. Ziolek, Glycerol oxidation on gold catalysts supported on group five metal oxides—a comparative study with other metal oxides and carbon based catalysts, Catal. Today 158 (2010) 121–129, https://doi.org/10.1016/j.cattod.2010.04.022.

[12] A. Villa, N. Dimitratos, C.E. Chan-Thaw, C. Hammond, L. Prati, G.J. Hutchings, Glycerol oxidation using gold-containing catalysts, Acc. Chem. Res. 48 (2015) 1403–1412, https://doi.org/10.1021/ar500426g.

[13] F.-F. Wang, S. Shao, C.-L. Liu, C.-L. Xu, R.-Z. Yang, W.-S. Dong, Selective oxidation of glycerol over Pt supported on mesoporous carbon nitride in base-free aqueous solution, Chem. Eng. J. 264 (2015) 336–343, https://doi.org/10.1016/j.cej.2014.11.115.

[14] M.L. Faroppa, M.E. Chiosso, J.J. Musci, M.A. Ocsachoque, A.B. Merlo, M.L. Casella, Oxidation of glycerol in base-free aqueous solution using carbon-supported Pt and PtSn catalyst, Catalysts 13 (2023) 1071, https://doi.org/10.3390/catal13071071.

[15] J. Lei, H. Dong, X. Duan, W. Chen, G. Qian, D. Chen, X. Zhou, Insights into activated carbon-supported platinum catalysts for base-free oxidation of glycerol, Ind. Eng. Chem. Res. 55 (2016) 420–427, https://doi.org/10.1021/acs.iecr.5b03076.

[16] E. Derrien, M. Mounguengui-Diallo, N. Perret, P. Marion, C. Pinel, M. Besson, Aerobic oxidation of glucose to glucaric acid under alkaline-free conditions: Au-based bimetallic catalysts and the effect of residues in a hemicellulose hydrolysate, Ind. Eng. Chem. Res. 56 (2017) 13175–13189, https://doi.org/10.1021/acs.iecr.7b01571.

[17] H. Shi, P.S. Thapa, B. Subramaniam, R.V. Chaudhari, Oxidation of glucose using mono- and bimetallic catalysts under base-free conditions, Org. Process. Res. Dev. 22 (2018) 1653–1662, https://doi.org/10.1021/acs.oprd.8b00302.

[18] N. Potrzebowska, L. Cardenas, E. Derrien, P. Marion, C. Pinel, M. Besson, N. Perret, Ultrasonication-assisted preparation of Au-Pt/ZrO_2 catalysts for the selective base-free oxidation of glucose to glucaric acid, ChemCatChem 16 (2024), https://doi.org/10.1002/cctc.202400338.

[19] P. Beltrame, M. Comotti, C. Della Pina, M. Rossi, Aerobic oxidation of glucose, Appl. Catal. A Gen. 297 (2006) 1–7, https://doi.org/10.1016/j.apcata.2005.08.029.

[20] T. Ishida, N. Kinoshita, H. Okatsu, T. Akita, T. Takei, M. Haruta, Influence of the support and the size of gold clusters on catalytic activity for glucose oxidation, Angew. Chem. Int. Ed. 47 (2008) 9265–9268, https://doi.org/10.1002/anie.200802845.

[21] U. Prüße, M. Herrmann, C. Baatz, N. Decker, Gold-catalyzed selective glucose oxidation at high glucose concentrations and oxygen partial pressures, Appl. Catal. A Gen. 406 (2011) 89–93, https://doi.org/10.1016/j.apcata.2011.08.013.

[22] R. Saliger, N. Decker, U. Prüße, d-Glucose oxidation with H2O2 on an Au/Al2O3 catalyst, Appl. Catal. B 102 (2011) 584–589, https://doi.org/10.1016/j.apcatb.2010.12.042.

[23] O. Reinsdorf, C. Pellegrin, C. Schmidt, M. Alvear, K. Eränen, D.Y. Murzin, T. Salmi, Selective oxidation of glucose using hydrogen peroxide as an oxidant: on the structure sensitivity of the apparent activation energy, ChemCatChem 15 (2023), https://doi.org/10.1002/cctc.202300536.

[24] Y. Önal, Structure sensitivity and kinetics of ?-glucose oxidation to ?-gluconic acid over carbon-supported gold catalysts, J. Catal. 223 (2004) 122–133, https://doi.org/10.1016/j.jcat.2004.01.010.

[25] S. Sadula, B. Saha, Aerobic oxidation of xylose to xylaric acid in water over Pt catalysts, ChemSusChem 11 (2018) 2124–2129, https://doi.org/10.1002/cssc.201800494.

[26] F. van der Klis, L. Gootjes, N.H. Verstijnen, J. van Haveren, D. Stephan van Es, J. H. Bitter, Carbohydrate structure–activity relations of Au-catalysed base-free oxidations: gold displaying a platinum lustre, RSC Adv. 12 (2022) 8918–8923, https://doi.org/10.1039/D2RA00255H.

[27] N.Lloyd. Johnson, Samuel Kotz, N. Balakrishnan, Continuous Univariate Distributions, Wiley, 1995.

[28] W. Xing, M. Yin, Q. Lv, Y. Hu, C. Liu, J. Zhang, Oxygen solubility, diffusion coefficient, and solution viscosity, in: Rotating Electrode Methods and Oxygen Reduction Electrocatalysts, Elsevier, 2014, pp. 1–31, https://doi.org/10.1016/B978-0-444-63278-4.00001-X.

[29] Dmitry Yu. Murzin, Tapio Salmi, Catalytic kinetics, 2nd ed., Elsevier Science, 2016.

[30] B.N. Zope, R.J. Davis, Inhibition of gold and platinum catalysts by reactive intermediates produced in the selective oxidation of alcohols in liquid water, Green Chem. 13 (2011) 3484, https://doi.org/10.1039/c1gc15953d.

[31] J. Lee, B. Saha, D.G. Vlachos, Pt catalysts for efficient aerobic oxidation of glucose to glucaric acid in water, Green Chem. 18 (2016) 3815–3822, https://doi.org/10.1039/C6GC00460A.

[32] N. Dimitratos, A. Villa, D. Wang, F. Porta, D. Su, L. Prati, Pd and Pt catalysts modified by alloying with Au in the selective oxidation of alcohols, J. Catal. 244 (2006) 113–121, https://doi.org/10.1016/j.jcat.2006.08.019.

[33] R.V. Mom, A. Knop-Gericke, Hydroxylation of platinum surface oxides induced by water vapor, J. Phys. Chem. Lett. 13 (2022) 879–883, https://doi.org/10.1021/acs.jpclett.1c03927.

[34] W.C. Ketchie, M. Murayama, R.J. Davis, Promotional effect of hydroxyl on the aqueous phase oxidation of carbon monoxide and glycerol over supported Au catalysts, Top. Catal. 44 (2007) 307–317, https://doi.org/10.1007/s11244-007-0304-x.

[35] W. Ketchie, M. Murayama, R. Davis, Selective oxidation of glycerol over carbon-supported AuPd catalysts, J. Catal. 250 (2007) 264–273, https://doi.org/10.1016/j.jcat.2007.06.011.

[36] Y. Cao, X. Liu, S. Iqbal, P.J. Miedziak, J.K. Edwards, R.D. Armstrong, D.J. Morgan, J. Wang, G.J. Hutchings, Base-free oxidation of glucose to gluconic acid using supported gold catalysts, Catal. Sci. Technol. 6 (2016) 107–117, https://doi.org/10.1039/C5CY00732A.

[37] E. Monti, A. Ventimiglia, L. Forster, E. Rodríguez-Aguado, J.A. Cecilia, F. Ospitali, T. Tabanelli, S. Albonetti, F. Cavani, I. Rivalta, C. D'Agostino, N. Dimitratos, Influence of stabilisers on the catalytic activity of supported Au colloidal nanoparticles for the liquid phase oxidation of glucose to glucaric acid: understanding the catalyst performance from NMR relaxation and computational studies, Green Chem. 25 (2023) 2640–2652, https://doi.org/10.1039/D2GC04418H.

[38] H.G.J. de Wilt, Part I. Oxidation of glucose to gluconic acid. Survey of techniques, Prod. R&D 11 (1972) 370–373, https://doi.org/10.1021/i360044a002.

[39] R.D. Armstrong, J. Hirayama, D.W. Knight, G.J. Hutchings, Quantitative determination of Pt-catalyzed <scp>d</scp> -glucose oxidation products using 2D NMR, ACS Catal. 9 (2019) 325–335, https://doi.org/10.1021/acscatal.8b03838.

[40] J. Dirkx, The oxidation of glucose with platinum on carbon as catalyst, J. Catal. 67 (1981) 1–13, https://doi.org/10.1016/0021-9517(81)90256-6.

[41] A. Savara, C.E. Chan-Thaw, J.E. Sutton, D. Wang, L. Prati, A. Villa, Molecular origin of the selectivity differences between Palladium and Gold–Palladium in benzyl alcohol oxidation: different oxygen adsorption properties, ChemCatChem 9 (2017) 253–257, https://doi.org/10.1002/cctc.201601295.